

SURFACE MORPHOLOGY AND WETTABILITY OF SEMICONDUCTING
IRON DISILICIDE



A THESIS SUBMITTED IN PARTIAL FULFILLMENT OF THE REQUIREMENT FOR THE
DEGREE OF MASTER OF SCIENCE IN APPLIED PHYSICS
DEPARTMENT OF PHYSICS
FACULTY OF SCIENCE
KING MONGKUT'S INSTITUTE OF TECHNOLOGY LADKRABANG
2018
KMUTL-2018-SC-M-030-049

This material is reserved for educational use only, not allowed for commercial use.

Forbidden to modify the content, and cite the document when use.



COPYRIGHT 2018

FACULTY OF SCIENCE

KING MONGKUT'S INSTITUTE OF TECHNOLOGY LADKRABANG

This material is reserved for educational use only, not allowed for commercial use.

Forbidden to modify the content, and cite the document when use.

Thesis Title	Surface Morphology and Wettability of Semiconducting Iron Disilicide
Student Name	Mr. Peerasil Charoenyuenyao
Student ID	59605078
Degree	Master of Science
Department	Physics
Year	2018
Thesis Advisor	Asst. Prof. Dr. Nathaporn Promros

Abstract

This research was separated into 2 parts. For the first part, semiconducting iron disilicide (β -FeSi₂) films were epitaxially formed on Si(111) wafers via facing-targets direct-current sputtering (FTDCS) at a substrate temperature of 600 °C. The as-created β -FeSi₂ films were annealed in a vacuum for 2 hours at 200 °C, 400 °C and 600 °C. From the field emission scanning electron microscopy (FESEM) and atomic force microscope (AFM) images, the surface morphology of the as-created β -FeSi₂ films demonstrated the existence of a porous area and root mean square (rms) roughness of 2.02 nm. The FESEM images for all annealed β -FeSi₂ films showed similarities in the film surface. The rms roughness values for the β -FeSi₂ films after annealing were nearly the same as those for the as-produced β -FeSi₂ films. The average contact angle for the surface of the as-created β -FeSi₂ films exhibited hydrophobic properties with a contact angle value of 98.7°. The contact angle decreased to 82.15° at an annealing temperature of 600 °C. For the second part, nanocrystalline (NC) FeSi₂ films were created by FTDCS at room temperature. The NC-FeSi₂ films were annealed at different temperatures of 300, 600, and 900 °C under high vacuum for 2 hours. From FESEM micrographs, the unannealed NC-FeSi₂ film surface consisted of numerous amounts of small uniform crystallites with diameters of 6-7 nm. Small uniform crystallites were merged into larger NC clusters at an annealing temperature of 300 °C. They were clustered and formed into larger clusters at annealing temperatures higher than 300 °C. According to the AFM micrograph, the unannealed NC-FeSi₂ films showed rms roughness of 0.81 nm. The rms roughness of the NC-FeSi₂ films was increased by annealing. The average contact angle of the unannealed NC-FeSi₂ film surface was 100.1°, which is hydrophobic. The NC-FeSi₂ film surface reached a maximum contact angle of 106.2° when the annealing temperature was increased to 300 °C. As annealing temperatures were increased to higher than 300 °C, the contact angles were reduced.

Keywords : Annealing, β -FeSi₂, Hydrophobic, NC-FeSi₂ , Wettability

This material is reserved for educational use only, not allowed for commercial use.

Forbidden to modify the content, and cite the document when use.

Acknowledgements

I would like to express my sincere gratitude to my advisor Asst. Prof. Dr. Nathaporn Promros for the support of my M.SC. study and research and the reformation of this thesis.

I am also thankful to Asst. Prof. Dr. Boonchoat Paosawatyanong for his kindness and valuable advice to develop myself in present and future.

I wish to acknowledge to the thesis committees: Assoc. Prof. Sarai Lekchaum, Asst. Prof. Dr. Boonchoat Paosawatyanong, and Asst. Prof. Dr. Prathan Buranasiri for offering their valuable time, support, direction throughout the modification of this thesis

Further, I am sincerely thankful to my parents for their supporting and advising me.

Lastly, I would like to thank to my senior, Mr. Pongsapak Sittimart, for his suggestion.

Mr. Peerasil Charoenyuenyao

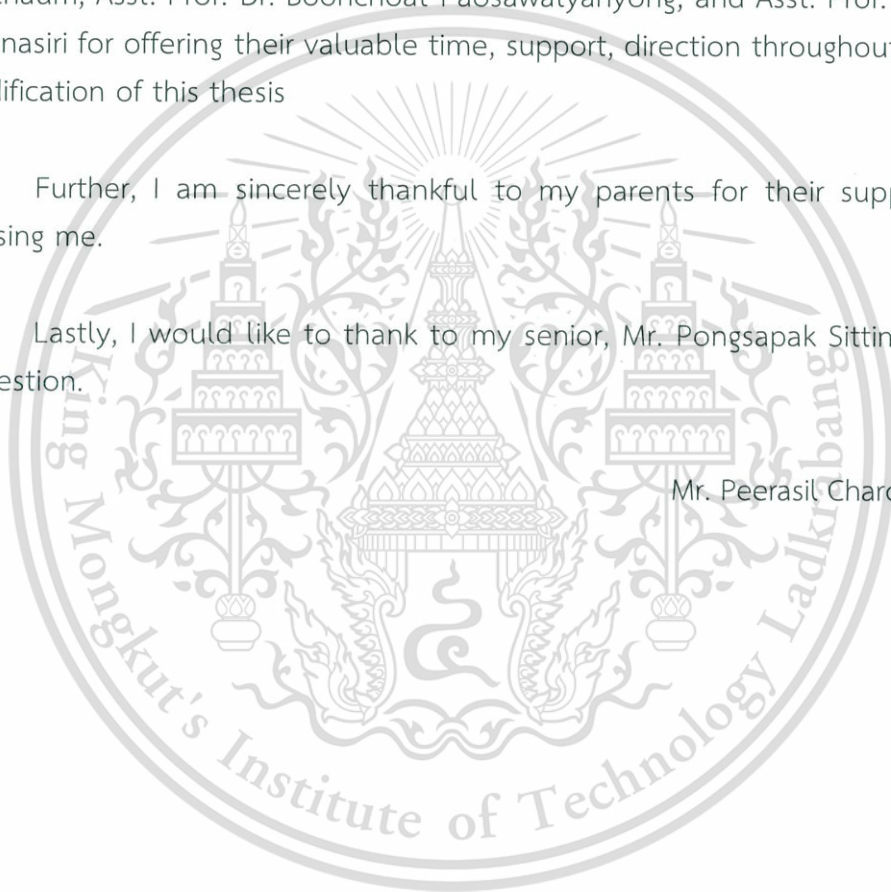


Table of Contents

	Page
Abstract in English	i
Acknowledgements.....	ii
Table of Contents	iii
List of Tables	vi
List of Figures.....	vii
Chapter 1 Introduction.....	1
1.1 Signification of the research	1
1.2 Purposes of the study.....	2
1.3 Scopes of the study	3
1.4 Research organization	3
1.5 Benefits of the study.....	4
Chapter 2 Theory and Literature Reviews	5
2.1 The properties of β -FeSi ₂	5
2.1.1 Physical features of β -FeSi ₂	5
2.2 The properties of NC-FeSi ₂	9
2.2.1 Physical features of NC-FeSi ₂	9
2.3 Deposition method.....	11
2.3.1 Facing-target direct-current sputtering (FTDCS).....	11
2.4 Wettability of surface.....	12
2.4.1 Contact angle.....	13
2.4.1 Wetting model of Wenzel and Cassie-Baxter.....	14
2.5. Heat treatment.....	15
2.5.1 Step of heat treatment.....	15
2.5.2 Annealing.....	16
2.6 Related research	16
2.6.1 Effect of post-annealing treatment on the wetting, optical and structural properties of Ag/Indium tin oxide thin films prepared by electron beam evaporation technique.....	16
2.6.2 Effect of annealing temperature on wettability of TiO ₂ nanotube array films	17
2.6.3 Structural and optical properties of Fe _{1-x} M _x Si ₂ thin films (M=Co, Mn; 0 ≤ x ≤ 0.20).....	18
Chapter 3 Research methodology.....	20
3.1 Creation of β -FeSi ₂ and NC-FeSi ₂ films	20
3.1.1 Production of β -FeSi ₂ on Si(111) wafer substrates.....	20

Table of Contents (cont.)

3.1.2 Production of NC-FeSi ₂ on Si(111) wafer substrates	21
3.2 Thermal annealing apparatus.....	22
3.2.1 Preparation of samples for annealing.....	23
3.3 Annealing process	24
3.3.1 Pre-heating	25
3.3.2 Annealing of sample	28
3.4 Characterization of the properties of as-produced and annealed films	29
3.4.1 XRD and pole figure pattern	29
3.4.2 Raman spectroscopy.....	30
3.4.3 Surface morphology of films.....	31
3.4.4 Surface roughness of the films	32
3.4.5 Contact angle measurement	32
Chapter 4 Results and Discussion.....	34
4.1 Physical properties of as-produced β -FeSi ₂ films	34
4.1.1 XRD and pole-figure pattern of as-produced β -FeSi ₂ films.....	34
4.1.2 Raman spectra of as-produced β -FeSi ₂ films	36
4.1.3 FESEM image of as-produced β -FeSi ₂ films.....	37
4.1.4 AFM image of as-produced β -FeSi ₂ films.....	38
4.1.5 Wettability of the as-produced β -FeSi ₂ films	39
4.2 Physical properties of unannealed and annealed β -FeSi ₂ films	40
4.2.1 Raman spectra of unannealed and annealed β -FeSi ₂ films	40
4.2.2 FESEM of as-produced and annealed β -FeSi ₂ films.....	41
4.2.3 AFM images of unannealed and annealed β -FeSi ₂ films.....	42
4.2.4 Wettability of as-produced and annealed β -FeSi ₂ film surface....	43
4.3 Physical properties of as-produced NC-FeSi ₂ films	44
4.3.1 XRD pattern of as-produced NC-FeSi ₂ films	44
4.3.2 Raman spectrum of as-produced NC-FeSi ₂ films	45
4.3.3 Raman lines of as-created NC-FeSi ₂ films produced by FTDCS and PLD.....	45
4.3.4 AFM image of as-produced NC-FeSi ₂ films	47
4.3.5 Wettability of the surface of as-produced NC-FeSi ₂ films.....	48
4.4 Physical properties of as-created and annealed NC-FeSi ₂ films	49
4.4.1 XRD patterns of as-created and annealed NC-FeSi ₂ films.....	49
4.4.2 Raman spectra of the as-created and annealed NC-FeSi ₂ films...	50
4.4.3 FESEM images of the as-produced and annealed NC-FeSi ₂ films	51
4.4.4 AFM images of as-produced and annealed NC-FeSi ₂ films.....	52

Table of Contents (cont.)

4.4.5 Wettability of the surface of as-created and annealed NC-FeSi ₂ films	53
Chapter 5 Summary and Suggestions for Future Work	55
5.1 Summary	55
5.2 Suggestions	56
References.....	57
Author Biography	64



List of Tables

Table	Page
1.1 Research procedures	3
3.1 Conditions for the production of β -FeSi ₂ films.....	21
3.2 Conditions for the creation of NC-FeSi ₂ films	22
3.3 Annealing conditions for the β -FeSi ₂ and NC-FeSi ₂ films	28



List of Figures

Figure	Page
2.1 Phase diagram of the Si-Fe system.....	6
2.2 Primitive cell of orthorhombic β -FeSi ₂ structure	6
2.3 Band diagram of β -FeSi ₂	7
2.4 Absorption spectrum for β -FeSi ₂ . The inset presents the interpolate indirect and direct optical band gaps of β -FeSi ₂	7
2.5 Two different types of epitaxial relationships for β -FeSi ₂ on Si(111).....	8
2.6 XRD patterns of NC-FeSi ₂ films formed via PLD and FTDCS. The inset of Fig. 2.6 is the micro-area electron diffraction (MD) pattern of the NC-FeSi ₂ film produced via PLD.....	10
2.7 The Dark-field TEM image of the NC-FeSi ₂ thin films formed via PLD.....	10
2.8 The schematic diagram of the FTDCS system.....	11
2.9 Illustration of contact angles on a smooth surface of substrate.....	12
2.10 The illustration of the liquid shape on the smooth surface substrate in different range of contact angle	13
2.11 Illustration of contact line for liquid on a flat surface	13
2.12 The illustration of (a) Wenzel interface and (b) Cassie-Baxter interface.....	14
2.13 SEM images of as-deposited and annealed Ag surface.....	16
2.14 XRD pattern of as-deposited and annealed Ag/ITO films.	17
2.15 Images of water drops on surface of as-deposited and annealed Ag/ITO films.....	17
2.16 XRD patterns of unannealed and annealed TN films.....	18
2.17 SEM surface images of and inset of water contact angle of (a) unannealed, (b) 200 °C, (c) 400 °C, (d) 600 °C, and (e) 800 °C annealed TN films	18
2.18 XRD pattern of β -FeSi ₂ , Fe _{0.8} Co _{0.2} Si ₂ , and Fe _{0.8} Co _{0.2} Si ₂	19
2.19 Raman spectra of (a) β -FeSi ₂ , (b) Fe _{0.9} Co _{0.1} Si ₂ , (c) Fe _{0.8} Co _{0.2} Si ₂ , (d) Fe _{0.9} Mn _{0.1} Si ₂ , (e) Fe _{0.8} Mn _{0.2} Si ₂ , (f) Fe _{0.8} Mn _{0.2} Si ₂ , and (g) MnSi _{1.7}	19
3.1 FTDCS system for the production of β -FeSi ₂ and NC-FeSi ₂ films.....	20
3.2 Thermal annealing apparatus for annealing the β -FeSi ₂ and NC-FeSi ₂ films.....	23
3.3 The example of annealing samples which placed on semi-cylinder quartz	23
3.4 Images of (a) the sample in the middle of the quartz tube and (b) the assembled part of the lid and open-side of the annealing tube.....	24
3.5 The panel of the cooling system	24
3.6 On-off switch for each part in the annealing apparatus	25
3.7 Tubomolecular pump (LEYBOLD TW70H).....	25
3.8 Status LED light of the turbomolecular pump for the apparatus	26

This material is reserved for educational use only, not allowed for commercial use.

Forbidden to modify the content, and cite the document when use.

List of Figures (cont.)

Figure	Page
3.9 Pressure gauge (CONBIVAC CM31) on the annealing apparatus.....	26
3.10 Temperature controller (Shimaden SR53) on the annealing apparatus.....	27
3.11 Temperature controller at 40 °C of pre-heat temperature.....	27
3.12 The as-produced and annealed β -FeSi ₂ films	28
3.13 The as-produced and annealed NC-FeSi ₂ films.....	28
3.14 XRD apparatus (RINT2000/PC) for investigation of epitaxial production and crystallinity of the films.....	29
3.15 XRD diffractometer (Rigaku, TTRAX III) at MTEC	30
3.16 Dispersive Raman spectroscopy (Bruker, SENTERA).....	30
3.17 An example of (a) the surface of sample and (b) the incident 532 nm laser toward the films during the measurement of the Raman spectrum.....	31
3.18 The Carl Zeiss Auriga FESEM apparatus.....	31
3.19 AFM apparatus (Park system, XE-120).....	32
3.20 Contact angle analyzer (OCA 20) and a display monitor.....	33
3.21 Drop on the surface of films in (a) normal view and (b) view on the monitor with an estimation of contact angle values.....	33
4.1 XRD pattern for as-created β -FeSi ₂ films on Si(111) substrates measured in 2θ - θ scan. The inset of Figure 4.1 reveals the XRD pattern measured in a 2θ scan with an incidence angle of 4°.....	34
4.2 Pole-figure pattern of as-produced β -FeSi ₂ films on Si(111) substrate.....	35
4.3 Raman lines of as-produced β -FeSi ₂ films formed by FTDCS method	36
4.4 FESEM image in plane surface view of β -FeSi ₂ films with 50K of magnitude....	37
4.5 AFM image of the surface of as-produced β -FeSi ₂ films	38
4.6 Contact angle between the water droplet and surface of the produced β -FeSi ₂ films.....	39
4.7 Typical Raman spectra for the β -FeSi ₂ films without annealing and at different annealing temperatures.....	40
4.8 Plane view FESEM micrographs for as-produced β -FeSi ₂ films at and after annealing at 200, 400, and 600 °C.....	41
4.9 AFM images of the β -FeSi ₂ films in the case of non-annealing and annealing under various temperatures (200 °C, 400 °C and 600 °C)	42
4.10 Contact angle images for as-produced β -FeSi ₂ films and β -FeSi ₂ films annealed at 200, 400, and 600 °C	43
4.11 XRD patterns of the as-produced NC-FeSi ₂ films formed by means of FTDCS and PLD, at a fixed incidence angle of 4°.....	44

List of Figures (cont.)

Figure	Page
4.12 Raman lines of as-created NC-FeSi ₂ films produced by FTDCS and PLD	45
4.13 FESEM surface of the produced NC-FeSi ₂ layer formed via (a) FTDCS and (b) PLD method, with 200,000 of magnitude.....	46
4.14 Cross-sectional view of the unannealed NC-FeSi ₂ interface formed via FTDCS	47
4.15 Illustrated AFM of the surface of unannealed NC-FeSi ₂ thin films	48
4.16 Images of water droplet on the surface of the NC-FeSi ₂ film surface.....	48
4.17 XRD pattern of the as-produced and annealed NC-FeSi ₂ films	49
4.18 Raman spectra of annealed NC-FeSi ₂ films under various annealing temperatures, compared with as-produced NC-FeSi ₂ films.....	50
4.19 FESEM images in plane surface view of as-created NC-FeSi ₂ films and after annealing at temperatures of 300 °C, 600 °C, and 900 °C	51
4.20 Cross-sectional view of as-created NC-FeSi ₂ films and after annealing at temperatures of 300 °C, 600 °C, and 900 °C.....	52
4.21 AFM images of the NC-FeSi ₂ films surface in case of non-annealing and annealing temperature of 300, 600, and 900 °C.....	53
4.22 Contact angles of as-produced and annealed NC-FeSi ₂ films (300 °C, 600 °C and 900 °C).....	54

Chapter 1

Introduction

1.1 Signification of the research

Lately, semiconducting iron disilicide (β -FeSi₂) has received significant attention because of its promising physical properties [1,2]. It has previously been confirmed that β -FeSi₂ can be epitaxially grown on Si substrates. The lattice mismatches for epitaxial growth between Si substrates and β -FeSi₂ layers ranged from 2 to 5 % [3,4]. More importantly, this compound is created from Si and Fe, which are environmentally friendly elements that are abundant in nature [5]. Additionally, the compound possesses indirect (0.76 eV) and direct (0.85 eV) optical band gaps. An absorption coefficient was found to be more than 10^5 cm^{-1} at 1.2 eV [6-8]. Additionally, it was previously proven that the surface of β -FeSi₂ films was smooth [9]. These properties of β -FeSi₂ are very suitable for utilization in applications for optoelectronic devices and hydrophobic surfaces. Previously, the creation of β -FeSi₂ films on Si(111) wafer substrates was accomplished via facing-targets direct-current sputtering (FTDCS) with a maintained substrate temperature of 600 °C [9]. The created β -FeSi₂ films displayed n-type properties and a carrier concentration of approximately $5 \times 10^{17} \text{ cm}^{-3}$ [9]. The resultant p-type Si/n-type β -FeSi₂ heterostructure can be employed in photodiode applications [10]. Even though the β -FeSi₂ films hold desirable features for hydrophobic surface applications, there have been no reports on β -FeSi₂ film surface concerning their wettability for employment in such applications. Therefore, the purpose of the current research was to study the surface morphology and wettability of β -FeSi₂ films. It was expected that the β -FeSi₂ film surface would be hydrophobic. Namely, the contact angle of the water on the β -FeSi₂ film surface would be greater than 90°. In addition, the β -FeSi₂ films were annealed under various annealing temperatures in order to provide the characteristics for the surface morphology and wettability of β -FeSi₂ films after being annealed. It was anticipated that the wettability of the β -FeSi₂ film surface would be modified by the annealing process.

It has been studied and reported that FeSi₂ in nanocrystalline (NC) structures holds several distinctive points similar to those of β -FeSi₂, thereby making it a potential candidate as a coating material for hydrophobic surfaces as well as optoelectronic devices [11,12]. The structure is comprised of crystals with diameters of less than 10 nm. It can be created on various substrates at room temperature [12-15]. The compound NC-FeSi₂ is produced from Fe and Si, which are environmentally friendly elements that are non-toxic and plentiful in nature [16,17].

Furthermore, NC-FeSi₂ has indirect and direct optical band gaps of 0.74 and 0.85 eV, respectively, which correspond to telecommunication wavelengths [18,19]. It also has a large absorption coefficient greater than 10⁵ cm⁻¹ at 1.2 eV [20]. Owing to the properties mentioned above, it may be possible to employ NC-FeSi₂ as a hydrophobic coating material as well as for application in photodiodes.

Several researchers have reported on the production of NC-FeSi₂ and FeSi₂ precipitates. The creation of nano-sized β-FeSi₂ precipitates was studied by Grimaldi et al. [21]. Nakamura et al. studied and reported on the epitaxial growth of FeSi₂ nanodots utilizing the creation of Fe on Si nanodots as well as the creation of β-FeSi₂ nanodots on Si(111) substrates using the co-deposition of Si and Fe [22,23]. In previous research, NC-FeSi₂ films were created via pulsed laser deposition (PLD) [11], including FTDCS methods [24]. It has been demonstrated in previous research that NC-FeSi₂ films have n-type conduction and a residual carrier density of around 10¹⁹ cm⁻³. The nanostructure of NC-FeSi₂ films has been studied and confirmed by transmission electron microscopy (TEM) [11] and field-emission scanning electron microscopy (FESEM) [16]. The p-type Si/n-type NC-FeSi₂ heterojunctions were formed and their electrical properties were investigated for usage in optoelectronic devices [12,19]. Despite the existence of a variety of previous studies, there have been few reports on NC-FeSi₂ film surfaces concerning their surface morphology and wettability properties until now. Thus, it was extremely challenging to study the surface morphology and wettability of NC-FeSi₂ films created via FTDCS. In this study, the surface morphology and wettability of NC-FeSi₂ films created via FTDCS were studied. It was expected that the surface of the NC-FeSi₂ films would show hydrophobicity. In other words, the water contact angle on the NC-FeSi₂ film surface would be greater than 90°. Additionally, the effect of annealing on the surface morphology and wettability of NC-FeSi₂ films was studied. We expected that the wettability of NC-FeSi₂ films would be changed by annealing under various annealing temperatures.

1.2 Purposes of the study

- 1) To study the surface morphology and wettability of as-produced β-FeSi₂ and NC-FeSi₂ films.
- 2) To study the impact of annealing temperature on the surface morphology and wettability of β-FeSi₂ and NC-FeSi₂ films.

1.3 Scopes of the study

- 1) By means of FTDCS, β -FeSi₂ films were produced at a substrate temperature of 600 °C and NC-FeSi₂ films were created at room temperature.
- 2) The β -FeSi₂ films were annealed at different annealing temperatures of 200, 400, and 600 °C in a vacuum.
- 3) The NC-FeSi₂ films were annealed under various annealing temperatures of 300, 600, and 900 °C in a vacuum.
- 4) The surface morphology and wettability of the β -FeSi₂ and NC-FeSi₂ films in the case of non-annealing and annealing under various temperatures were investigated.

1.4 Research organization

Table 1.1 Research procedures

Procedure	Period				
	Jul-Sep	Oct-Nov	Dec-Jan	Fab-Mar	Apr
Study the corresponding article to the research topic	←—————→				
Investigate the surface morphology and wettability of the as-produced films		←—————→			
Conduct thermal annealing of the as-produced films		←—————→			
Characterize the surface morphology and wettability of the films after annealing			←—————→		
Organize the topic for each chapter and write down the thesis			←—————→		

1.5 Benefits of the study

- 1) Demonstrate the surface morphology and wettability of as-produced β -FeSi₂ and NC-FeSi₂ films created via FTDCS.
- 2) Provide the characteristics for surface morphology and wettability of β -FeSi₂ and NC-FeSi₂ films after annealing.



Chapter 2

Theory and Literature Reviews

This chapter reviews the essential background for discussing the physical properties of β and NC-FeSi₂ as well as the basic concepts of wettability properties. It starts with a discussion of β -FeSi₂ properties and the epitaxial production of β -FeSi₂ on Si(111). The semiconducting properties of NC-FeSi₂ are then discussed. Next, the backgrounds of the deposition method, wettability, and annealing are described. Previously published papers related to this study are discussed and compared with the current research.

2.1 The properties of β -FeSi₂

2.1.1 Physical Features of β -FeSi₂

Figure 2.1 displays a phase diagram for the Fe-Si system. It can be seen that there are several phases including the intermediate phase (Fe₅Si₃), metal-rich silicide (Fe₃Si), monosilicide (FeSi), and disilicide (FeSi₂). In the area of the FeSi₂, three phases are separated as follows: cubic (γ -FeSi₂), orthorhombic (β -FeSi₂), and tetragonal (α -FeSi₂) [25]. The cubic γ -FeSi₂ phase is a metastable, low-temperature phase that appears during polymorphic transformation of β -FeSi₂ at 650 °C. The metallic α -FeSi₂ phase is stable when temperature is > 950 °C. It can be transformed into the orthorhombic β -FeSi₂ phase when the temperature is < 950 °C [26,27]. Recently, β -FeSi₂, which is a semiconductor, has attracted significant attention because of its potential material application in optoelectronic devices [28,29]. β -FeSi₂ is comprised of Fe and Si, which are environmentally friendly, non-toxic, and plentiful in nature [30,31]. The compound holds an orthorhombic structure having 48 atoms per unit cell (Si 32 atoms and Fe 16 atoms) and the lattice parameters of $c = 0.788$ nm, $b = 0.778$ nm, and $a = 0.986$ nm, as depicted in Fig. 2.2. The unit cell possesses two inequivalent Fe sites, each occupied by 8 atoms and two inequivalent Si sites with 16 atoms in each [32].

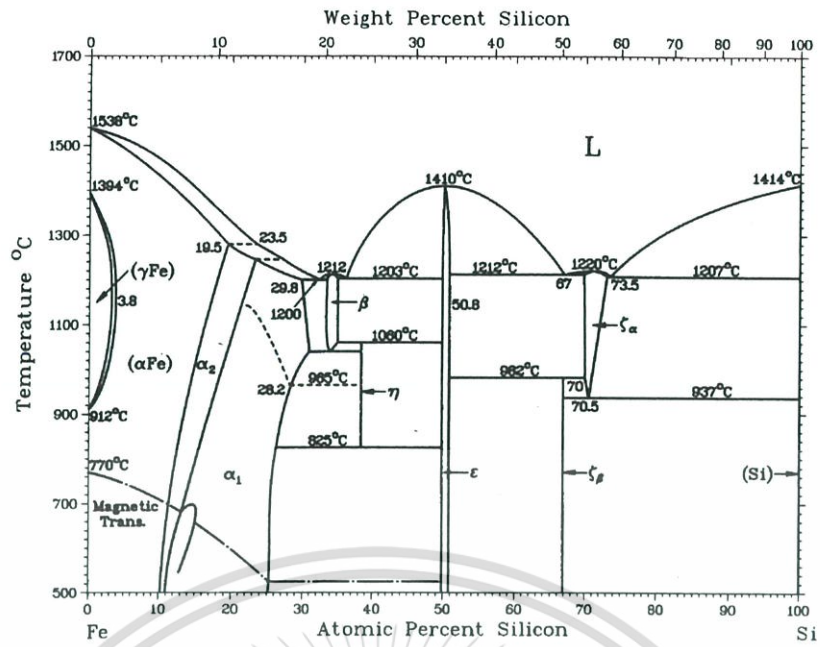


Figure 2.1 Phase diagram of the Si-Fe system [25].

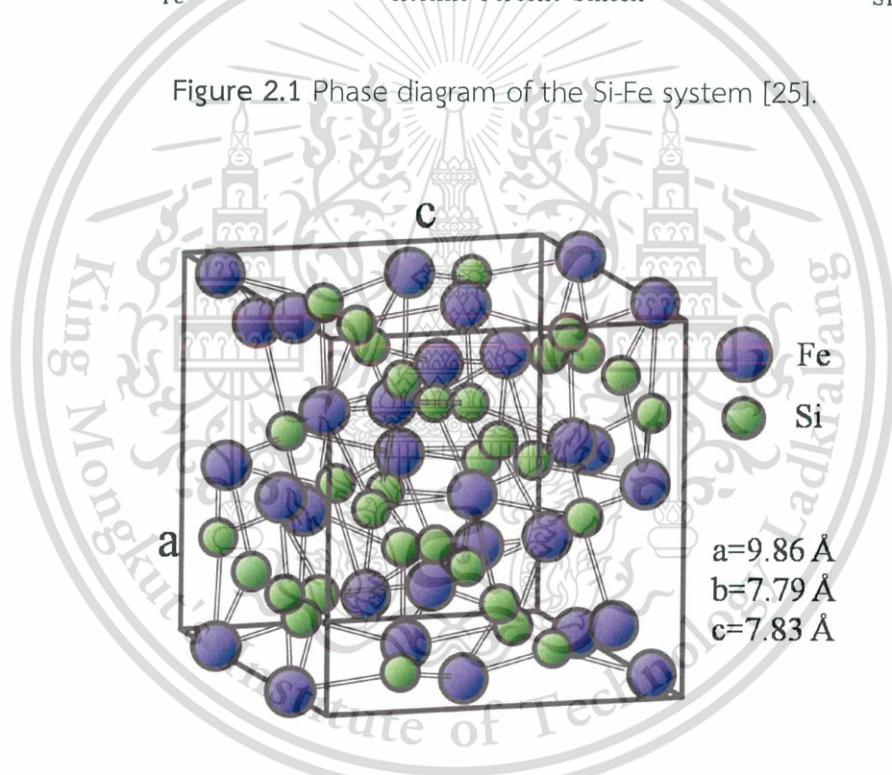


Figure 2.2 Primitive cell of orthorhombic β -FeSi₂ structure.

Figure 2.3 displays a band diagram of β -FeSi₂ for energy close to the band gap. The nature of the gap in the band structure is indirect, as displayed in Fig. 2.4. The difference between the calculated direct (Γ) and indirect gaps is quite small. An indirect gap could explain the part of absorption found for energy below the direct-gap transition energy [32]. As shown in the inset of Fig. 2.4, β -FeSi₂ possesses an indirect band gap of around 0.76 eV, which is below the direct optical band gap of 0.85 eV and corresponds to optical fiber for telecommunication wavelengths [8,9,33]. Specifically, its large optical absorption coefficient is greater than 10^5 cm^{-1} . This value of absorption coefficient is at least two orders of magnitude higher than that of crystalline Si at 1.2 eV, as illustrated in Fig. 2.4 [34,35].

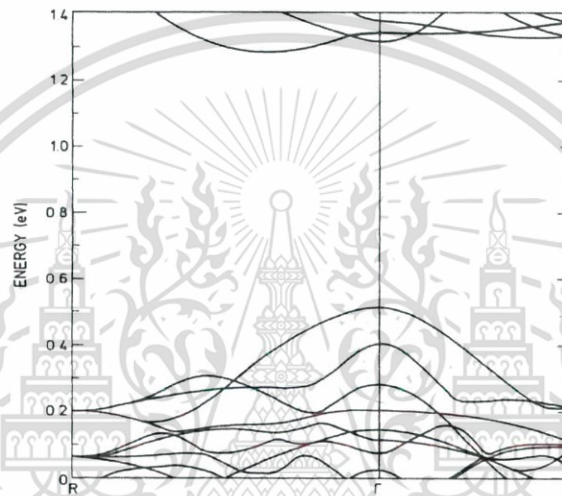


Figure 2.3 Band diagram of β -FeSi₂ [32].

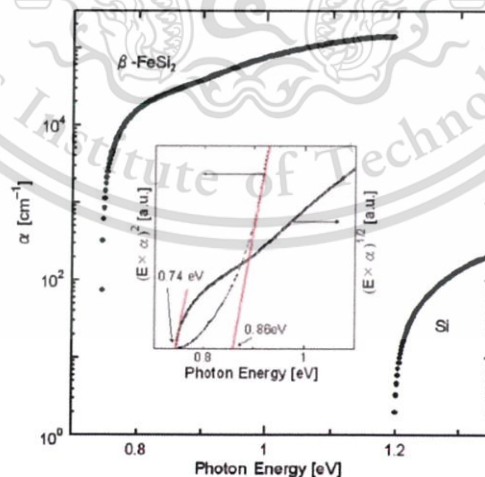


Figure 2.4 Absorption spectrum for β -FeSi₂. The inset presents the interpolated indirect and direct optical band gaps of β -FeSi₂ [33].

The heterostructures between β -FeSi₂ and Si can be formed by the epitaxial growth of β -FeSi₂ films on Si substrates. In the current study, the lattice mismatches for this epitaxial growth were from 2 to 5% [5,36]. For the growth of β -FeSi₂ on Si(111), the two epitaxial relationships are FeSi₂ (110)/Si(111) with FeSi₂ [001]||Si $\langle 110 \rangle$ and FeSi₂ (101)/Si(111) with FeSi₂ [010]||Si $\langle 011 \rangle$ [37].

Figure 2.5 presents the three epitaxial variants for each of these two epitaxial relationships. For the epitaxial growth of β -FeSi₂ on Si(111), there is a second type of twinning that can occur. In addition to the possible azimuthal rotations of 120° among crystallographically equivalent directions of the substrate surface, there could be a rotation of 180° such that the β -FeSi₂ [001] direction [as-summing the (110) matching face] is along either Si[011] or Si[0 $\bar{1}1$]. A lattice mismatch was +1.4% (+2.0%) along Si $\langle 110 \rangle$ and -1.9% (-2.4) along Si $\langle 11\bar{2} \rangle$ [38].

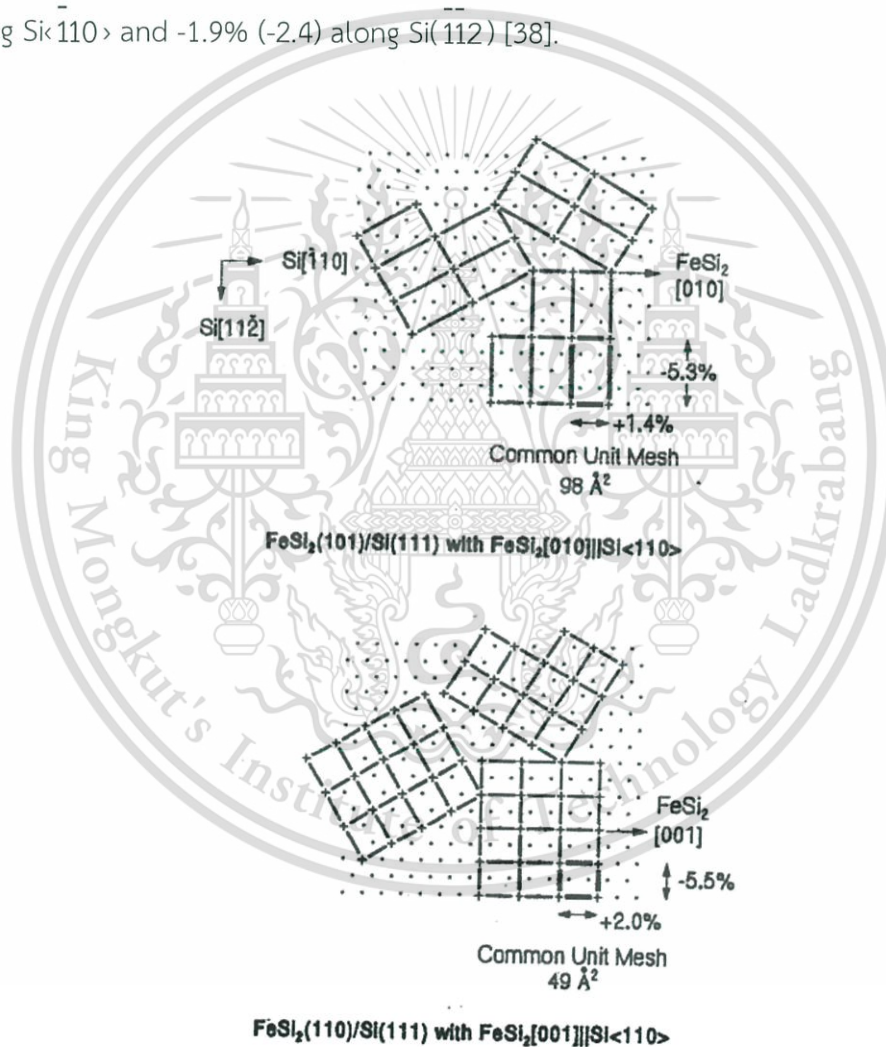


Figure 2.5 Two different types of epitaxial relationships for β -FeSi₂ on Si(111) [37].

2.2 The properties of NC-FeSi₂

2.2.1 Physical Features of NC-FeSi₂

A previous report was made by M. Milosavljevic et al. concerning the discovery of an amorphous form of FeSi₂ [39]. A homogenous amorphous FeSi₂ layer was produced via ion-beam mixing (IEM) of Fe layers onto Si at 300 °C utilizing Ar⁸⁺ ions. The measurements of optical absorption revealed a semiconductor with a direct band gap of around 0.88 eV. Rapid diffusion of Si to the surface was assigned as the dominating process that resulted in the creation of amorphous FeSi₂ [40]. Previously, NC-FeSi₂ films were successfully created via PLD employing FeSi₂ targets, after which their physical properties were investigated [11]. In recent years, NC-FeSi₂ has become a promising candidate for use in near-infrared (NIR) semiconductors and coating materials [41]. It exhibits physical properties close to those of β -FeSi₂ as well as amorphous FeSi₂ [42,43]. Further, it is comprised of environmentally friendly elements (Fe and Si) that are naturally abundant and nontoxic [24]. It is a semiconductor that possesses an optical band gap of 0.87 eV [12] and its absorption coefficient is found to be more than 10^5 cm^{-1} at 1.2 eV [21,44]. Notably, NC-FeSi₂ films can be created on a variety of substrates that are made of various types of solids at room temperature [19]. In previous research, NC-FeSi₂ films produced by means of PLD [11] and FTDCS [24] were structurally examined by usage of X-ray diffraction (XRD) and TEM. Figure 2.6 depicts the XRD patterns for the NC-FeSi₂ films produced via PLD and FTDCS. These XRD patterns were measured in the mode of 2θ -scan at a fixed incidence angle of 4° . A broad peak appeared at 2θ between 40° and 50° . This broad peak is likely due to the nanocrystalline structure of the NC-FeSi₂ films. Basically, β -FeSi₂ has many crystalline planes for diffraction, such as 422, 511, 313, 331, 004, 040, 114, and 133, at 2θ between 40° and 50° . The broad peak might be resultant from the overlapping of the diffractions from these crystalline planes. The peak intensity for the NC-FeSi₂ films created via FTDCS was slightly enhanced compared to that of NC-FeSi₂ films produced by means of PLD. This suggests that the crystallite diameters of the NC-FeSi₂ films created via FTDCS are slightly larger than those of the NC-FeSi₂ films produced through PLD. The pattern of micro-area electron diffraction (MD) for the NC-FeSi₂ films produced via PLD demonstrates the weak and broad ring, as depicted in the inset of Figure 2.6. Its radius corresponds to the lattice spacing of 2.03 Å. This is consistent with the acquired XRD result, in which a weak and broad peak was found at 2θ between 40° and 50° . Figure 2.7 presents a dark-field image for the NC-FeSi₂ film produced via PLD using the broad ring. The NC-FeSi₂ films produced through PLD are comprised of many crystallites with diameters between 3-5 nm. This might be a nanocrystalline of β -FeSi₂.

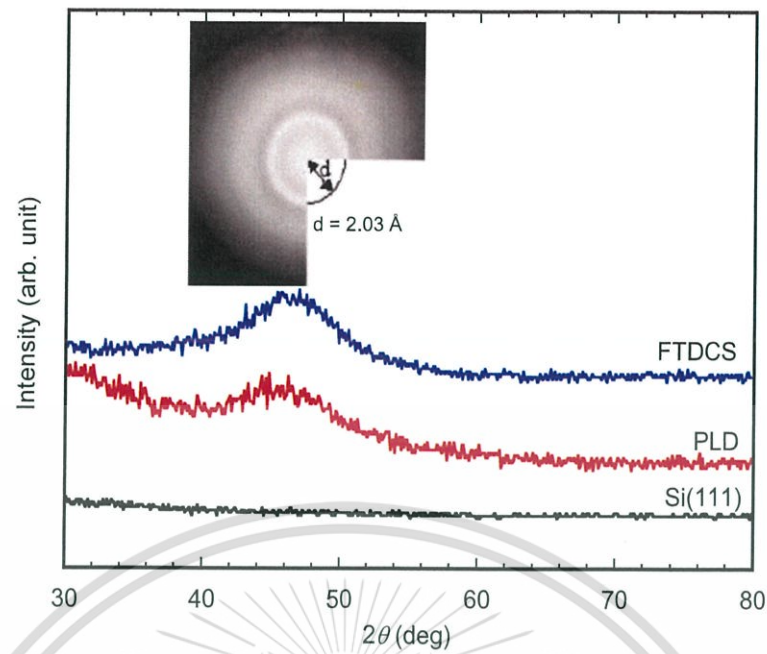


Figure 2.6 XRD patterns of NC-FeSi₂ films formed via PLD and FTDCS. The inset of Fig. 2.6 is the micro-area electron diffraction (MD) pattern of the NC-FeSi₂ film produced via PLD [11,24].



Figure 2.7 The Dark-field TEM image of the NC-FeSi₂ thin films formed via PLD [11].

2.3 Deposition method [45]

Sputtering is a physical vapor deposition (PVD) process that is utilized for the growth of thin film layers as well as cleaning and etching of the surface of the film or surface. This process is generated by the bombardment of accelerated ions on the surface of a sputtering target. After the accelerated ions reach the surface of the target with energy above the surface binding energy, a target atom can be ejected from a target and deposited on a substrate.

2.3.1 Facing-target direct-current sputtering (FTDCS) [4,9,46-48]

FTDCS is a modified sputtering system having the advantages of low-substrate temperature and high deposition rate during sputtering. A schematic of the FTDCS system is shown in Figure 2.8. The FTDCS system consists of two circular-shaped targets with the same dimension. Each target is situated opposing the other. Permanent magnets are arranged in a division behind the pair of targets to form a magnetic field spreading from one target to the other. Such a magnetic field confines plasma, generated by a discharge process, within the discharge area. A sputtering particle formed by the discharge process is deposited on a substrate attached in isolation from the discharge space.

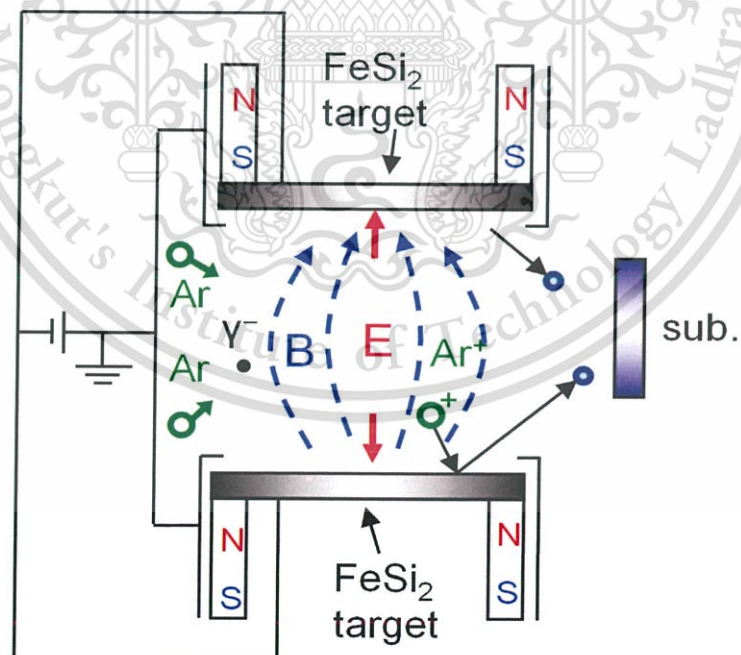


Figure 2.8 The schematic diagram of the FTDCS system.

FTDCS has the following advantages: (i) high plasma density generated from the sputtering process; (ii) sputtering at low pressure operation; (iii) low increment of substrate temperature; (iv) low damage from plasma; and (v) acquired films with low difference stoichiometry in comparison with a target owing to the substrate being free of plasma. Besides, the energy of particles that reach the surface of the substrate is higher when compared to the use of other methods due to sputtering at low pressure.

2.4 Wettability of surface [49]

Figure 2.9 presents a liquid drop located on a solid surface. In this case, the contact angle is defined as the angle determined by the intersection of the liquid-solid interface (γ_{sl}), and the liquid-vapor interface (γ_{lv}) (geometrically earned by employing a tangent line from the contact area that closes to the γ_{lv} in the droplet contour). In Figure 2.9, the three phases of the contact line are shown, representing solid, liquid, and vapor. A small contact angle is noticeable when the liquid flattens on the exterior layer of the substrate, while a high contact angle is noted when the liquid forms on the surface in round-shape.

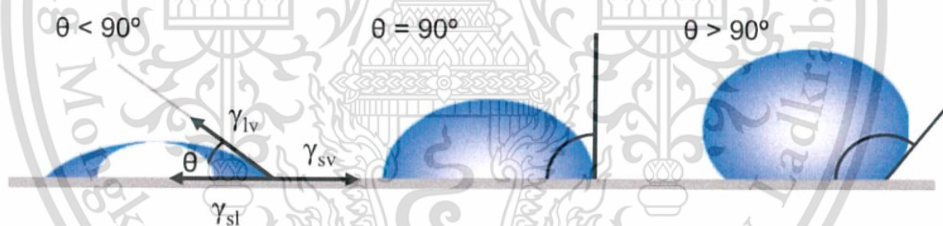


Figure 2.9 Illustration of contact angles on a smooth surface of substrate [49].

The material surface was indicated as a hydrophilic surface where the contact angle values between the drop and contact area of the surface were in a range from 5° to 90° . Namely, the drop will cover a large area on the surface. When the values of contact angle range from 90 to 150° , it can be determined that the surface is hydrophobic. In other words, the contact area between the water droplets is minimal, resulting in maintaining the drop in a sphere. In the case of contact angles evaluated in excess of 150° , the contact surface is shown to have nearly no contact between the drops, called a “Superhydrophobic surface”. Conversely, the surface will show superhydrophilic properties where the contact angle values are lower than 5° . In this case, the drop is almost covering the entire contact regime of the substrate

surface and showing a flat-shape for the drop on the substrate surface. The wetting behavior of the surface is revealed in Figure 2.10.

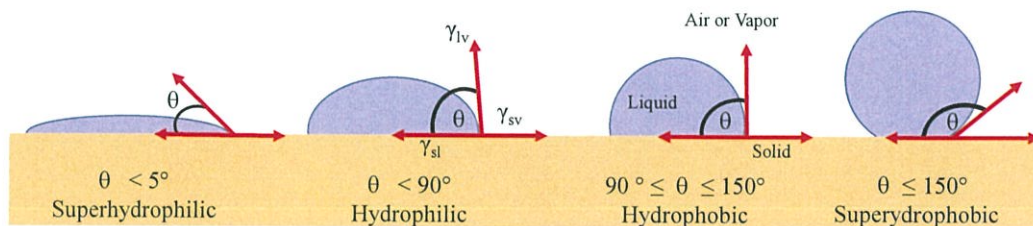


Figure 2.10 The illustration of the liquid shape on the smooth surface substrate in different range of contact angle.

2.4.1 Contact angle [50,51]

Atoms on a solid surface possess fewer bonds with neighboring atoms than those in the interior and, thus, have higher energy. This surface energy or surface tension (γ) is equal to the work required to produce a unit area of the surface at constant temperature and pressure. As displayed in Figure 2.11, when a liquid drop is placed in contact with a solid, the equilibrium of the solid surface will be established at a certain angle, called the static contact angle (θ_0), which is given by Young's equation:

$$\cos \theta_0 = \frac{\gamma_{sv} - \gamma_{sl}}{\gamma_{lv}} \quad (2.1)$$

Where γ_{sv} , γ_{sl} and γ_{lv} are the surface energies of the solid against air, solid against liquid and liquid against air, respectively.

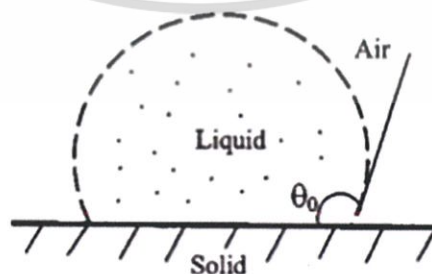


Figure 2.11 Illustration of contact line for liquid on a flat surface [51].

2.4.2 Wetting model of Wenzel and Cassie-Baxter [51-54]

In the case of a rough surface, two wetting models are usually seen: Wenzel's model and Cassie-Baxter's model. These two models are utilized for explanation of the contact angle between the drop and the rough surface, where the drop and air can infiltrate into the groove of the surface. The Wenzel and Cassie-Baxter interface are revealed in Figure 2.12 (a) and (b), respectively.

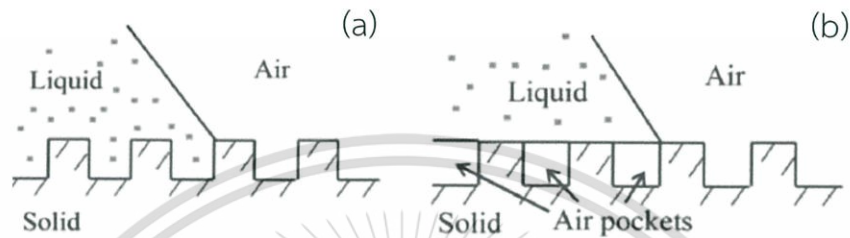


Figure 2.12 The illustration of (a) Wenzel interface and (b) Cassie-Baxter interface [51].

For the Wenzel model, the liquid drops infiltrate into the surface grooves, resulting in higher surface wettability because of the increase in contact area. Wenzel's model describes the contact angle (θ) with a rough surface by relating it to that of a flat solid surface. This model modifies Young's equation as follows:

$$\cos \theta_0 = r \left(\frac{\gamma_{sv} - \gamma_{sl}}{\gamma_{lv}} \right) = r \cos \theta \quad (2.2)$$

Where r is the non-dimensional surface roughness factor.

The r is defined by the ratio of the actual area of the rough surface to the flat projection area, as symbolized by A_{sl} and A_F , respectively.

$$r = \frac{A_{sl}}{A_F} \quad (2.3)$$

The Cassie-Baxter model explains that an air pocket occurs underneath the liquid drops, resulting in a larger contact angle. This model assumes a composite surface is comprised of two kinds of patches. The resulting equation is for the apparent contact angle on such a composite surface. Cassie-Baxter's model explains the contact angle with two parameters of fractional area (f), and contact angle (θ). The contact angle of this model is given by:

$$\cos \theta = f_1 \cos \theta_1 + f_2 \cos \theta_2 \quad (2.4)$$

Where
$$f_1 + f_2 = 1 \quad (2.5)$$

For composite interface, the first fraction corresponds to the solid-liquid interface, f_{sl} and $\theta_1 = \theta_0$. The second fraction corresponds to the liquid-air interface, $1 - f_{sl}$ and $\theta_2 = 180^\circ$. Combining (2.4) with (2.2), the Cassie-Baxter model can be presented as:

$$\cos \theta = f_{sl} \cos \theta_0 - 1 + f_{sl} \quad (2.6)$$

2.5 Heat treatment [55]

Heat treatment is the procedure of applying and reducing temperature on a material for the modification of desired properties. The features of materials are conditional on their structural aspects. The structures may be different in order of magnitude: macro-, micro-, nano-, or atomic scale. Typically, heat treatment may affect transformation in the defects of crystallite, which can modify the mechanical properties of the material. The changing of the structure for each material can be transformed depending on the treatment system.

2.5.1 Step of heat treatment

Generally, the process of heat treatment is accomplished in the following three steps:

1. Heating the sample with high temperature.
2. Retaining the treatment temperature for term.
3. Cooling the sample to room temperature or lower.

2.5.2 Annealing

Annealing is commonly a means of softening in which samples are heated to create the steadiness high-temperature state and then allowed to moderate very slowly. For certain purposes, annealing is the standard method for developing mechanical, structural, stress reduction of materials, and surface morphology modification of samples with temperature and time.

2.6 Related research

This section presents the related research of the effect of annealing on films properties from other research groups.

2.6.1 Effect of post-annealing treatment on the wetting, optical and structural properties of Ag/Indium tin oxide thin films prepared by electron beam evaporation technique [56]

Y. Azizian-Kalandaragh et.al. reported the effect of annealing on films properties of Ag/Indium Tin Oxide (ITO) under 100, 200, 300, and 400 °C in air, 1 hour. From SEM images, the films exhibited the gathering and a composition of Ag particles on the layer of a substrate. The XRD pattern of Ag/Indium tin oxide shows an improvement of film's crystalline, with higher intensity of peaks of Ag films. Conversely, the crystallinities of the Indium Tin Oxide film were not changed after annealing. The value of contact angle for as-deposited films was 92°. After annealing. The contact angle of the film surface was decreased.

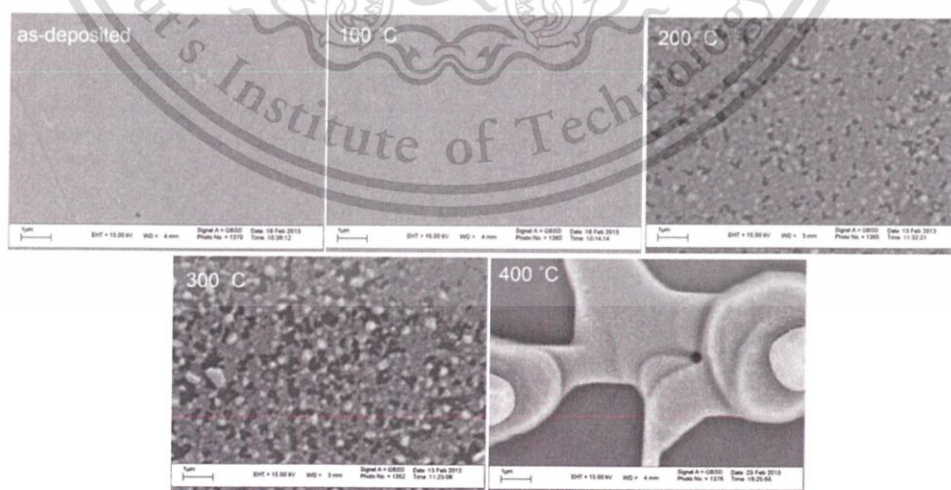


Figure 2.13 SEM images of as-deposited and annealed Ag surfaces. [56]

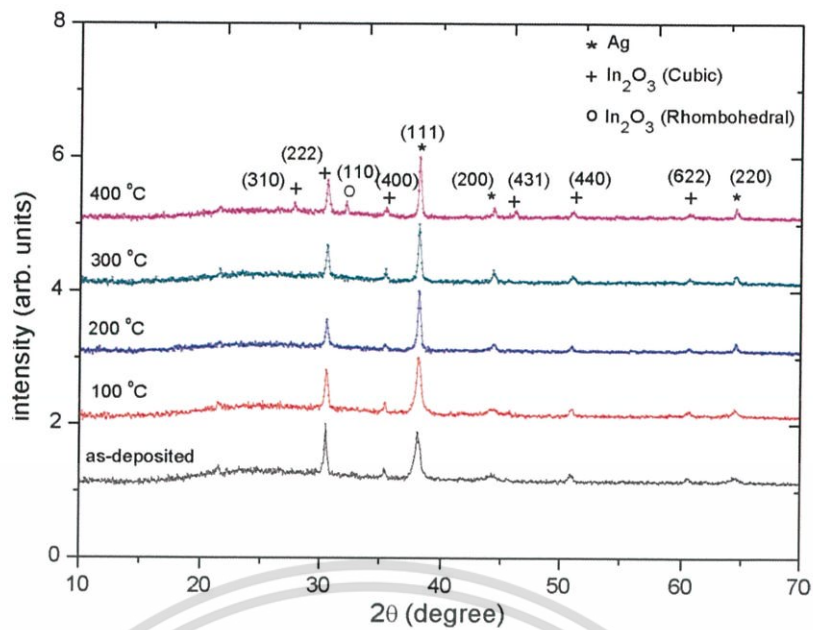


Figure 2.14 XRD pattern of as-deposited and annealed Ag/ITO films. [56]



Figure 2.15 Images of water drops on surface of as-deposited and annealed Ag/ITO films. [56]

2.6.2 Effect of annealing temperature on wettability of TiO₂ nanotube array films [57]

L. Yang et al. reported an impact of annealing temperature on wettability of TiO₂ nanotube array (TN) films. The TN films were annealed in air under annealing temperature of 200, 400, 600, and 800 °C, for 2 hours. From XRD pattern, the structure of TN films was changed from amorphous to anatase at annealing temperature of 400 °C and rutile with annealing temperature ranging from 600 to 800 °C. From SEM results, the TN structure are completely suffered after annealed under 800 °C. The contact angles were 130, 133, 135, and 134° for the unannealed films and annealed films at 200 °C, 400 °C, and 600 °C, respectively. At 800 °C, the drop on the film surface is spread over the surface of films, where the contact angle value was 77°.

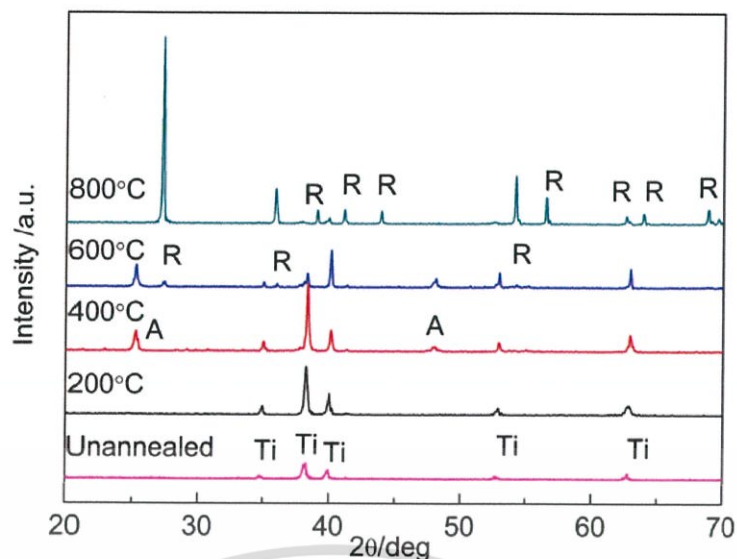


Figure 2.16 XRD patterns of unannealed and annealed TN films.

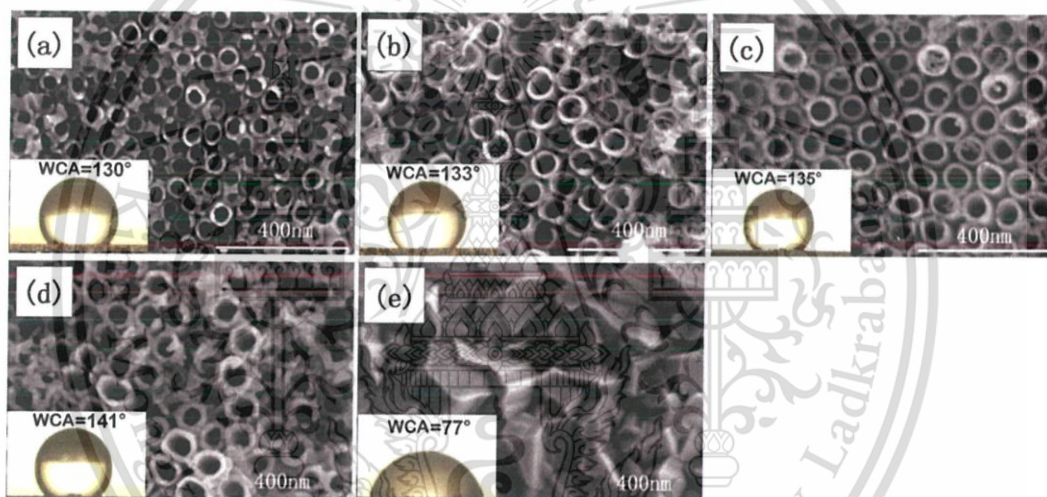


Figure 2.17 SEM surface images and inset of water contact angle of (a) unannealed, (b) 200 °C, (c) 400 °C, (d) 600 °C, and (e) 800 °C annealed TN films.

2.6.2 Structural and optical properties of $\text{Fe}_{1-x}\text{M}_x\text{Si}_2$ thin films (M=Co, Mn; $0 \leq x \leq 0.20$) [58]

M. Fanciulli et al. reported the structural and optical properties of Co or Mn alloying in $\beta\text{-FeSi}_2$ films. Via PLD, the films of Fe and Co or Mn were formed, at room temperature, onto Si(001) wafers and in-situ annealing at 700 °C. From the results, the XRD patterns show crystalline phase of the orthorhombic $\beta\text{-FeSi}_2$ type, as shown in Fig. 2.18. From Raman lines, the peaks of $\beta\text{-FeSi}_2$ films were found at a position of 244, 191, 197, 335, 487, 393, and 251 cm^{-1} . M. Fanciulli et al.

This material is reserved for educational use only, not allowed for commercial use.

Forbidden to modify the content, and cite the document when use.

reported that they observed the Red-shift of the lines, between 1 and 3 cm^{-1} . Further, broad peak is observed for films containing Co. The Raman lines of films were shown in Fig.2.19.

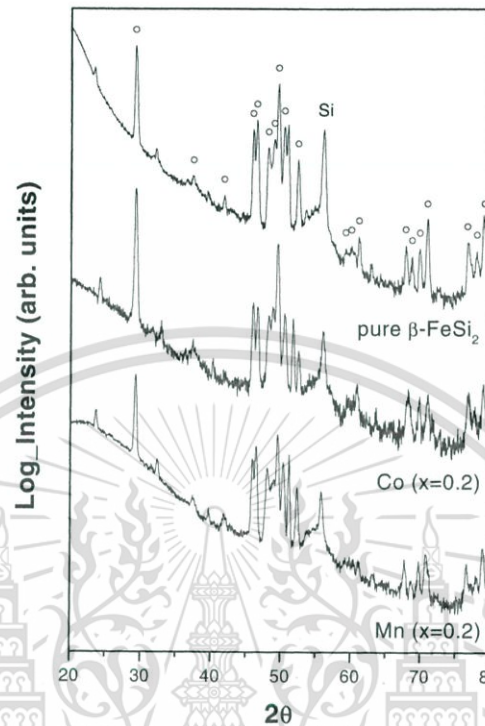


Figure 2.18 XRD pattern of $\beta\text{-FeSi}_2$, $\text{Fe}_{0.8}\text{Co}_{0.2}\text{Si}_2$, and $\text{Fe}_{0.8}\text{Mn}_{0.2}\text{Si}_2$. [58]

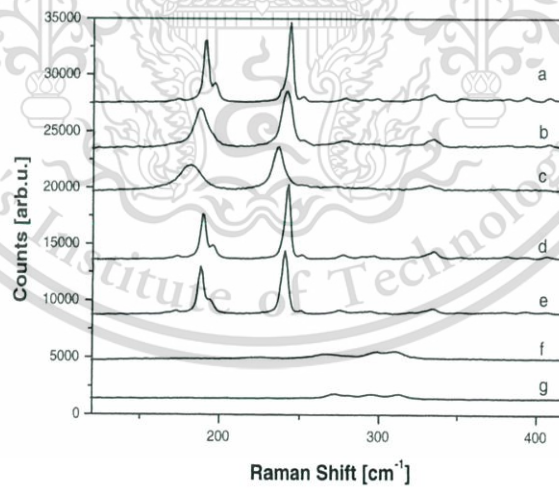


Figure 2.19 Raman spectra of (a) $\beta\text{-FeSi}_2$, (b) $\text{Fe}_{0.9}\text{Co}_{0.1}\text{Si}_2$, (c) $\text{Fe}_{0.8}\text{Co}_{0.2}\text{Si}_2$, (d) $\text{Fe}_{0.9}\text{Mn}_{0.1}\text{Si}_2$, (e) $\text{Fe}_{0.8}\text{Mn}_{0.2}\text{Si}_2$, (f) $\text{Fe}_{0.8}\text{Mn}_{0.2}\text{Si}_2$, and (g) $\text{MnSi}_{1.7}$.

Chapter 3

Research methodology

This chapter describes the details of film production, annealing and characterization of film properties. It begins by describing the conditions for the creation of the β -FeSi₂ and NC-FeSi₂ films by FTDCS. Next, the system and process for annealing of the films are described. The last section of this chapter provides the details of several measurement methods for characterization of the physical properties of the films.

3.1 Creation of β -FeSi₂ and NC-FeSi₂ films

In this research, β -FeSi₂ and NC-FeSi₂ films were formed onto the surfaces of Si(111) substrates by Asst. Prof. Dr. Nathapron Promros and Japanese students at Kyushu University, Japan. The FTDCS system for the production of β -FeSi₂ and NC-FeSi₂ films is illustrated in Figure 3.1.



Figure 3.1 FTDCS system for the production of β -FeSi₂ and NC-FeSi₂ films.

3.1.1 Production of β -FeSi₂ films on Si(111) wafer substrates

β -FeSi₂ films with a film thickness of 300 nm were produced on p-type Si(111) wafer substrates via FTDCS by utilizing a pair of FeSi₂ alloy targets. During the production of the β -FeSi₂ layer, the substrate temperature was maintained at 600 °C. The Si(111) wafer was cleaned by rinsing in acetone, methanol, and deionized water for five minutes in each step. Next, a diluted hydrofluoric (HF) acid solution (concentration of 1 %) was utilized to remove the oxide layer. The HF residue was purged instantaneously from the p-type Si wafer in deionized water. After cleaning,

This material is reserved for educational use only, not allowed for commercial use.

Forbidden to modify the content, and cite the document when use.

the Si(111) wafer was attached to the substrate holder inside the FTDCS chamber with 7.5 cm of space between the Si(111) wafer and target. The β -FeSi₂ films were formed on the Si(111) wafer substrates at a sputtering pressure of 1.33×10^{-1} Pa. The sputtering process was performed in Ar gas (purity: 6N). The flow rate of the argon gas was maintained at 15 sccm. The applied voltage for sputtering was assigned to 1 kV, while the created sputtering current was approximately 1.5 mA. The conditions for sputtering of the β -FeSi₂ films can be summarized as shown in Table 3.1.

Table 3.1 Conditions for the production of β -FeSi₂ films

Coating conditions for β -FeSi ₂ films	
Substrate	p-Si (111)
Target of sputtering	FeSi ₂ (Purity: 6N)
Temperature of substrate	600 °C
Target to substrate distance	7.5 cm
Base pressure	3×10^{-5} Pa
Ar gas flow rate	15 sccm
Sputtering pressure	1.33×10^{-1} Pa
Voltage	1000 V
Current	1.5 mA
Film thickness	300 nm

3.1.2 Production of NC-FeSi₂ films on Si(111) wafer substrates

By use of the FTDCS method, NC-FeSi₂ films with 350 nm of thickness were created on Si(111) wafer substrates at room temperature. Prior to the creation of the NC-FeSi₂ thin films, solvents were employed to clean off the oils and organic residues on the surfaces of the Si wafer substrates. Initially, the Si wafer substrates were cleaned with acetone. Then, they were transferred and cleaned by methanol. In the next step, they were transferred and cleaned with deionized water. Each cleaning step was carried out for a period of 5 minutes. Subsequently, HF (concentration: 1%) solution was employed to remove the native oxide layer from the surface of the Si wafer substrates. Each Si wafer substrate was dipped in HF solution and then was transferred and rinsed in deionized water. The cleaned Si substrate was then mounted on a substrate holder in an FTDCS apparatus. The inside of the chamber of the FTDCS apparatus was evacuated to a base pressure of 1×10^{-5} Pa. The NC-FeSi₂ thin creation was performed in an atmosphere consisting of Ar and H₂ mixed gases. The flow rates of Ar and H₂ gases were maintained at 15 and

10 sccm, respectively. During film creation under the operating pressure of 1.33×10^{-1} Pa, the applied direct current voltage and discharge current were 950 V and 1.2 mA, respectively. The conditions for sputtering of the NC-FeSi₂ films can be summarized as shown in Table 3.2.

Table 3.2 Conditions for the creation of NC-FeSi₂ films

Coating conditions for NC-FeSi ₂ films	
Substrate	p-Si (111)
Target of sputtering	FeSi ₂ (Purity: 6N)
Temperature of substrate	Room temperature
Base pressure	1×10^{-5} Pa
Sputtering pressure	1.33×10^{-1} Pa
Ar gas flow rate	15 sccm
H ₂ gas flow rate	10 sccm
Discharge voltage	950 V
Discharge current	1.2 mA
Film thickness	350 nm

3.2 Thermal annealing apparatus

In the current research, the β -FeSi₂ and NC-FeSi₂ films produced via FTDCS method were annealed under various temperatures using an annealing apparatus at Photonics Technology Laboratory (PTL), National Electronics and Computer Technology Center (NECTEC), Thailand. The annealing apparatus is shown in Figure 3.2. This apparatus consists of five parts: cooling system, evacuate system, gas feeding system, heat source, and controlling system. The film surfaces of the produced β -FeSi₂ and NC-FeSi₂ layers were modified by utilizing this annealing apparatus.

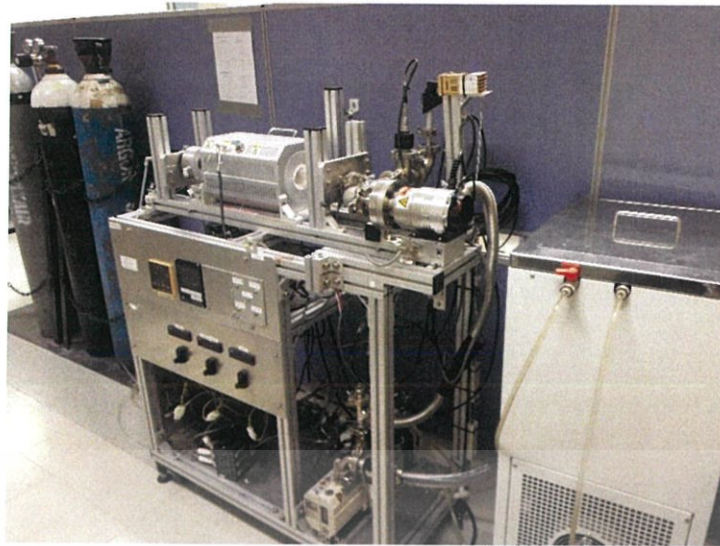


Figure 3.2 Thermal annealing apparatus for annealing the β -FeSi₂ and NC-FeSi₂ films.

3.2.1 Preparation of samples for annealing

Before loading samples into the furnace, the β -FeSi₂ and NC-FeSi₂ films were placed on semi-cylinder quartz, as shown in Figure 3.3, where the surface of the films was set in a face-up direction.



Figure 3.3 The example of annealing samples which placed on semi-cylinder quartz.

Next, the semi-cylinder quartz was placed at the center position of the annealing quartz tube, as shown in Figure 3.4(a). Subsequently, the open-side of the annealing quartz was assembled by the gas feeding lid, as demonstrated in Figure 3.4(b).

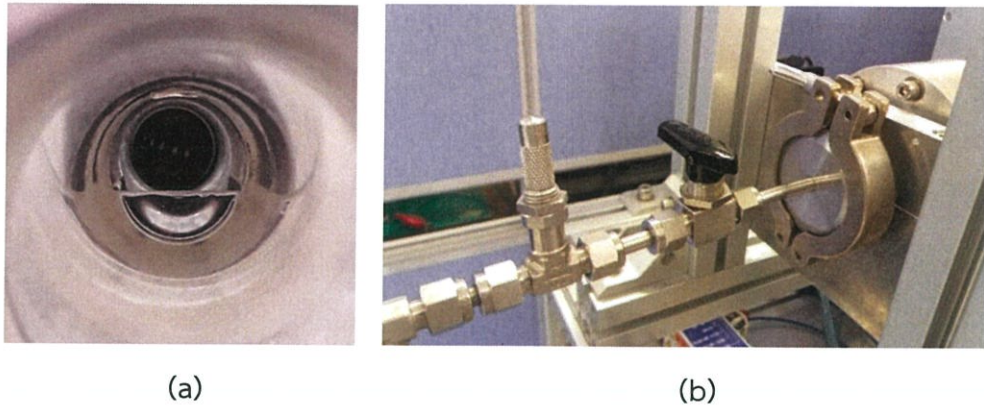


Figure 3.4 Images of (a) the sample in the middle of the quartz tube and (b) the assembled part of the lid and open-side of the annealing tube.

3.3. Annealing process

After the preparation of samples for annealing, the researcher switched on the main supply and turned on the cooling system, where the temperature of the water was set to approximately 20 to 25 °C, as shown in Figure 3.5. Subsequently, the “PUMP” button was pressed to begin the flow of cooling water into the apparatus.



Figure 3.5 The panel of the cooling system.

3.3.1 Pre-heating

Turn on the heater of the furnace and pressure gauge. Next, turn on the rotary to prepare the base pressure for annealing conditions. After the pressure inside the quartz tube reaches 5×10^{-2} mbar, turn on the switch for a turbomolecular pump, LEYBOLD TW70H, for pumping in the high-vacuum state, where the Status LED light will shine, and wait until the pressure decreases to 5×10^{-6} mbar.

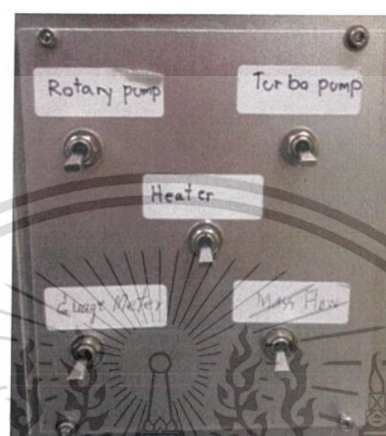


Figure 3.6 On-off switch for each part in the annealing apparatus.

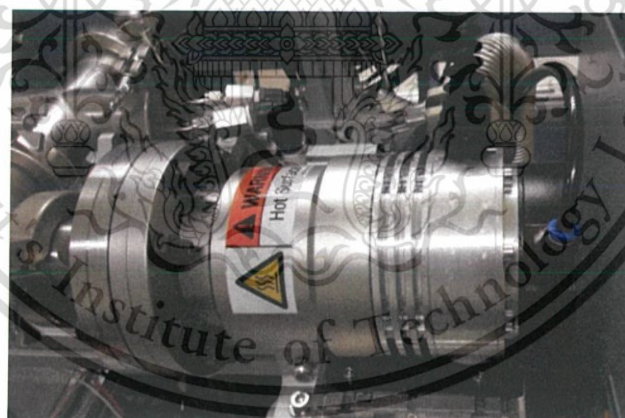


Figure 3.7 Turbomolecular pump (LEYBOLD TW70H)



Figure 3.8 Status LED light of the turbomolecular pump for the apparatus.

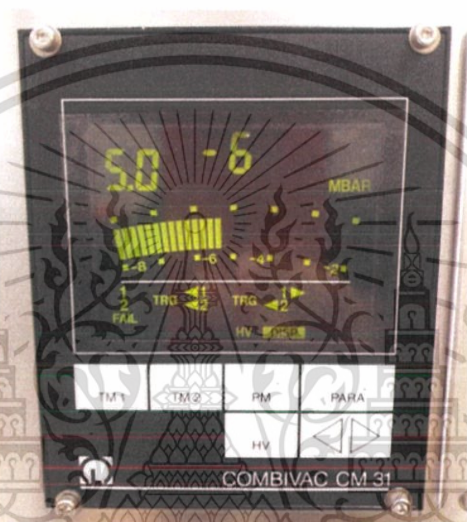


Figure 3.9 Pressure gauge (CONBIVAC CM31) on the annealing apparatus.

After achieving annealing pressure, the annealing temperature was controlled by the temperature controller (Shimaden SR53) on the apparatus, as shown in Figure 3.10. For controlling the annealing temperature, the controller was set up with the following steps: 1) press a digit selector to select the position of each numeral. 3) press “OK” to run the heating process. For pre-heating, the temperature was maintained at 40 °C for 10 minutes.

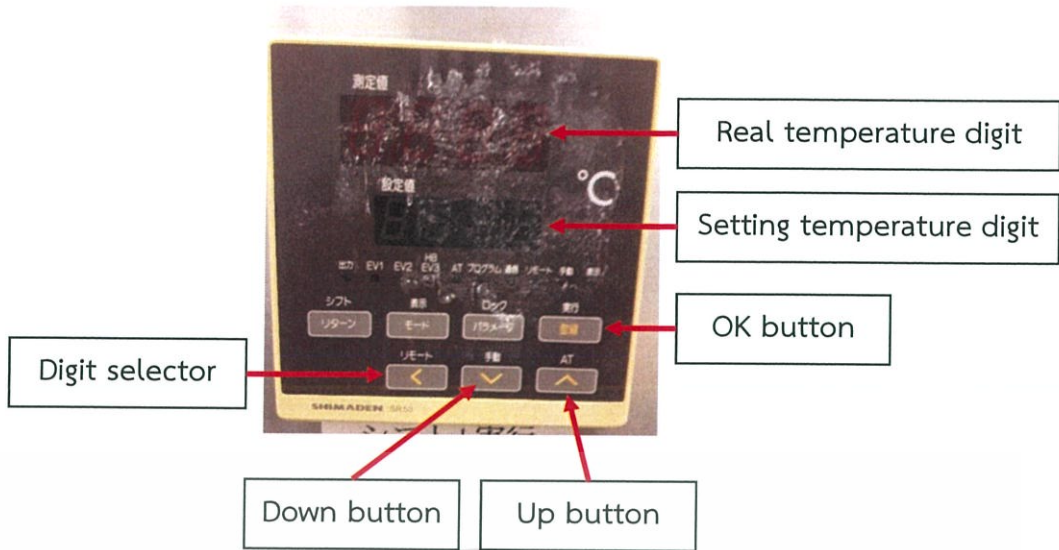


Figure 3.10 Temperature controller (Shimaden SR53) on the annealing apparatus.

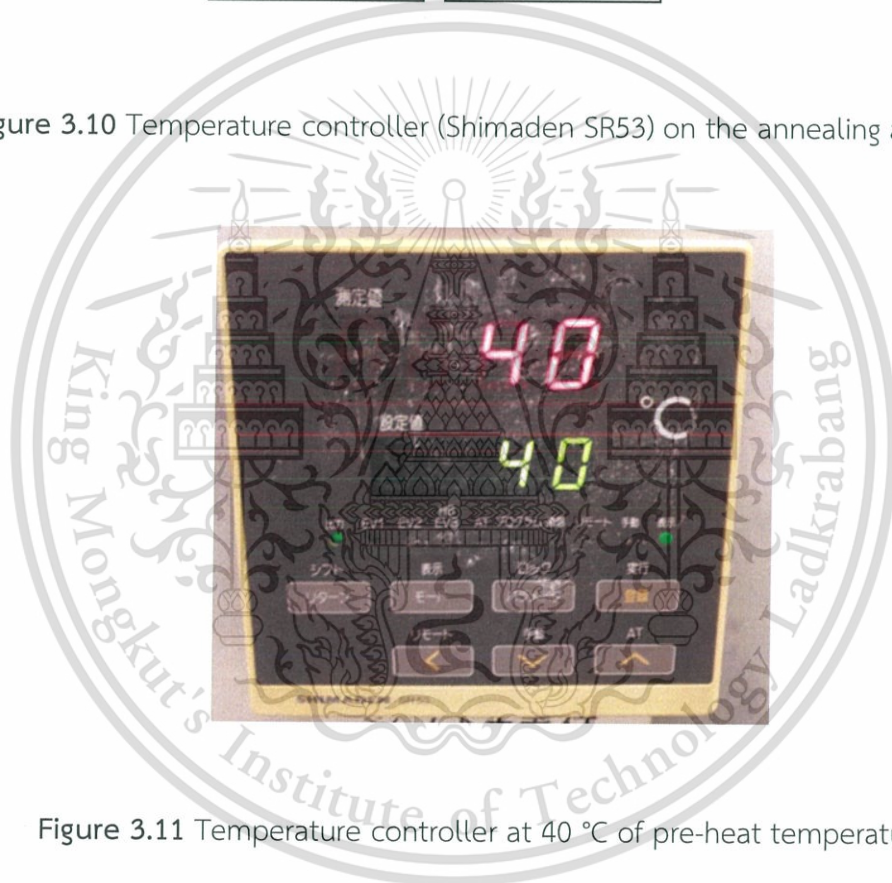


Figure 3.11 Temperature controller at 40 °C of pre-heat temperature.

3.3.2 Annealing of sample

Inside the quartz tube, the temperature was increased to 40 °C from the room temperature. After that, it was increased 20 °C at each step until it reached the desired temperature. Then, the temperature was kept constant for 2 hours in each annealing condition. The annealing conditions for all films are depicted in Table 3.3. The annealing temperatures for the β -FeSi₂ films were set to 200, 400, and 600 °C. For the NC-FeSi₂ films, the annealing temperatures were set to 300, 600, and 900 °C. The as-produced and annealed β -FeSi₂ and NC-FeSi₂ films are shown in Figure 3.12 and 3.13, respectively.

Table 3.3 Annealing conditions for the β -FeSi₂ and NC-FeSi₂ films

Materials	Annealing pressure (mbar)	Annealing temperature (°C)	Annealing time (hours)
β -FeSi ₂	$< 5 \times 10^{-6}$	200	2
β -FeSi ₂	$< 5 \times 10^{-6}$	400	2
β -FeSi ₂	$< 5 \times 10^{-6}$	600	2
NC-FeSi ₂	$< 5 \times 10^{-6}$	300	2
NC-FeSi ₂	$< 5 \times 10^{-6}$	600	2
NC-FeSi ₂	$< 5 \times 10^{-6}$	900	2



Figure 3.12 The as-produced and annealed β -FeSi₂ films.

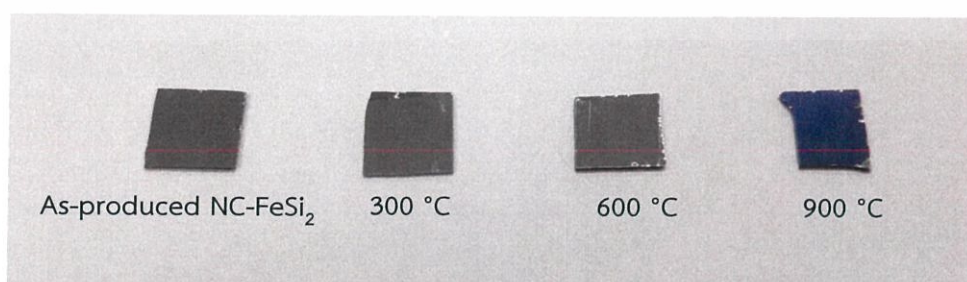


Figure 3.13 The as-produced and annealed NC-FeSi₂ films.

This material is reserved for educational use only, not allowed for commercial use.

Forbidden to modify the content, and cite the document when use.

3.4 Characterization of the properties of as-produced and annealed films.

Physical properties such as crystallinity, surface morphology, and wettability for the as-deposited and annealed films were characterized using the following measurements:

3.4.1 XRD and pole-figure patterns

The epitaxial production and crystallinity of the films were examined by utilization of XRD measurement using 2θ - θ and pole figure measurement techniques. These measurements were performed by XRD apparatus (RINT2000/PC) at Kyushu University, as shown in Figure 3.14. The 2θ - θ and pole figure patterns of the as-produced β -FeSi₂ and NC-FeSi₂ films were measured through this apparatus. The XRD patterns of as-produced and annealed NC-FeSi₂ films were characterized by XRD diffractometer (Rigaku, TTRAX III) at National Metal and Materials Technology Center (MTEC) as shown in Fig. 3.15.

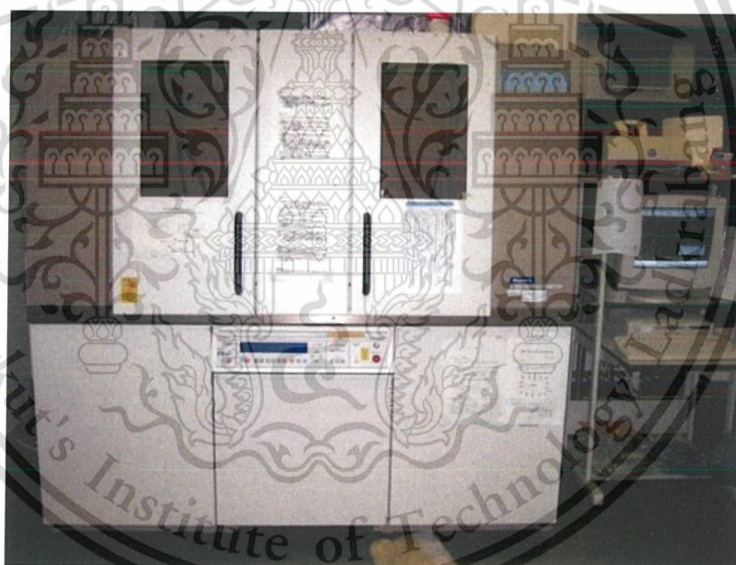


Figure. 3.14 XRD apparatus (RINT2000/PC) for investigation of epitaxial production and crystallinity of the films.



Figure. 3.15 The XRD diffractometer (Rigaku, TTRAX III) at MTEC.

3.4.2 Raman spectroscopy

The Raman spectra of the as-deposited and annealed films were monitored by means of dispersive Raman spectroscopy (Bruker, SENTERRA), as displayed in Figure 3.16. The Raman lines were energized by a 532 nm laser and detected with a high-sensitivity CCD detector, 1024 x 256 pixels, thermoelectrically cooled to $-70\text{ }^{\circ}\text{C}$ (ambient at $20\text{ }^{\circ}\text{C}$). The diameter of the laser spot was less than $1\text{ }\mu\text{m}$. The Raman lines of the sample were measured with 0.5 mW of laser power, $25\text{ }\mu\text{m}$ of detector aperture, and the spectral range of $50\text{ to }4450\text{ cm}^{-1}$, under integration time of 1 sec.

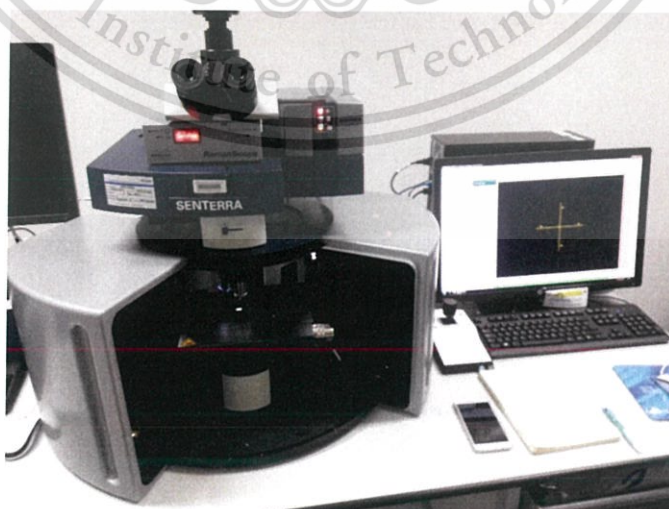


Figure 3.16 Dispersive Raman spectroscopy (Bruker, SENTERRA).

This material is reserved for educational use only, not allowed for commercial use.

Forbidden to modify the content, and cite the document when use.

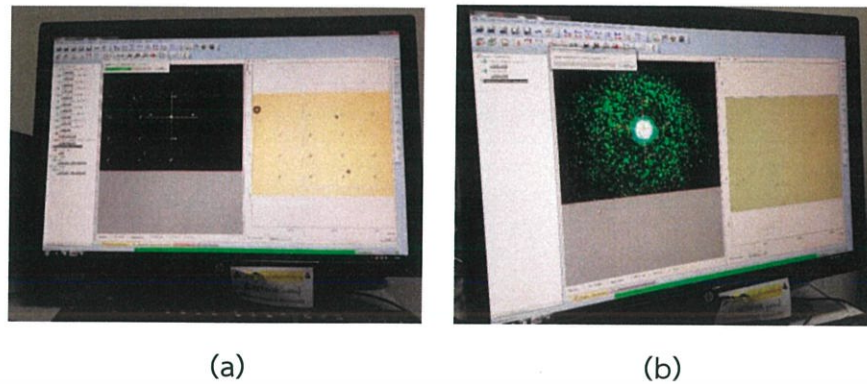


Figure 3.17 An example of (a) the surface of sample and (b) the incident 532 nm laser toward the films during the measurement of the Raman spectrum.

3.4.3 Surface morphology of the films

The plane surface views of the as-created and annealed β -FeSi₂ and NC-FeSi₂ films produced via FTDCS were displayed by utilizing a Carl Zeiss Auriga Field Emission Scanning Electron Microscope with magnitude in a range from 50k to 200k. Figure 3.18 displays the Carl Zeiss Auriga FESEM apparatus used for examination of the surface morphology of the as-created and annealed films.



Figure 3.18 The Carl Zeiss Auriga FESEM apparatus.

This material is reserved for educational use only, not allowed for commercial use.

Forbidden to modify the content, and cite the document when use.

3.4.4 Surface roughness of the films

The roughness of the surface for as-produced and annealed films was investigated by means of atomic force microscopy (AFM). Figure 3.19 illustrates the AFM apparatus (Park system, XE-120) for observing surface roughness. The surfaces of as-produced and annealed β -FeSi₂ and NC-FeSi₂ films were scanned in non-contact mode.

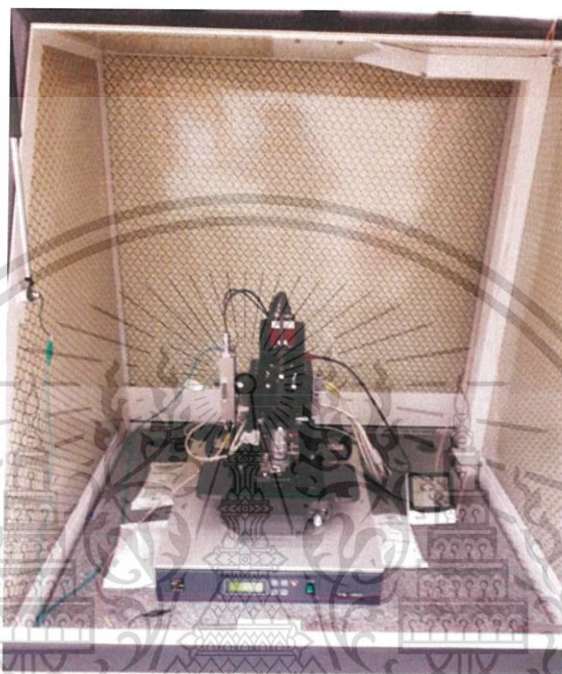


Figure 3.19 AFM apparatus (Park system, XE-120).

3.4.5 Contact angle measurement

To identify the wettability properties of the β -FeSi₂ and NC-FeSi₂ films before and after the annealing process, the contact angle values of dropped water on the surface of films were measured by contact angle OCA 20, as shown in Figure 3.20. In this measurement method, the DI water was dropped from a syringe with a volume of 10 μ l and dosing rate of 1 μ l/s. Images of the drop on the film surface were captured by a camera on the instrument. The contact angle values were analyzed through SCA 20 Software.

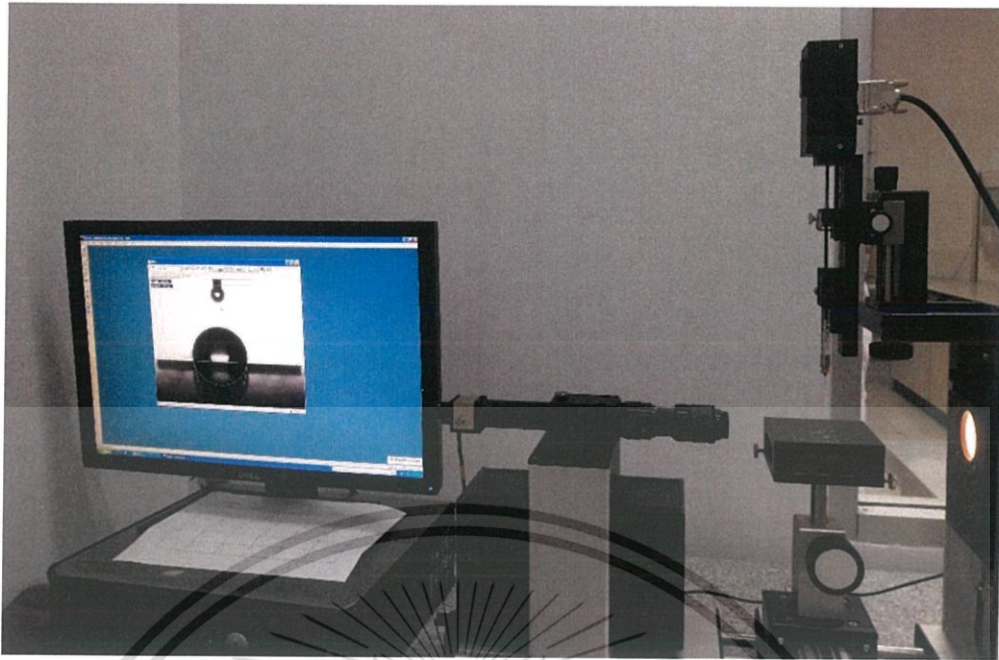


Figure 3.20 Contact angle analyzer (OCA 20) and a display monitor.



Figure 3.21 Drop on the surface of films in (a) normal view and (b) view on the monitor with an estimation of contact angle values.

Chapter 4

Results and Discussion

This chapter describes the experimental results of surface morphology, structural, and wetting properties for as-produced and annealed samples (β -FeSi₂ and NC-FeSi₂ thin films). The results of annealed films were compared to the as-produced films. The results are presented in a sequence of as-produced β -FeSi₂, annealed β -FeSi₂, as-produced NC-FeSi₂, and annealed NC-FeSi₂, respectively.

4.1 Physical properties of as-produced β -FeSi₂ films

4.1.1. XRD and pole-figure pattern of as-produced β -FeSi₂ films

Figure 4.1 presents the scanned XRD pattern for the as-produced β -FeSi₂ layer on the Si(111)-wafer substrates. Measurement of this XRD pattern was performed using an XRD apparatus (RINT2000/PC) at Kyushu University. With 2θ - θ scan, the scanned pattern of the layer exhibited intense 202/220 and weak 404/440 peaks at the positions of 29° and 60.48°, respectively. These peaks are essential for β -FeSi₂ films, which can explain that β -FeSi₂ films can be epitaxially created on Si(111) substrates. The inset of Fig. 4.1 reveals the XRD pattern, 2θ scan, of the as-produced β -FeSi₂ films. The inset in Figure 4 displays the XRD pattern in a 2θ scan with an incidence angle of 4°. The 2θ XRD pattern exhibited no peaks. Namely, no β phase diffraction peaks appeared in 2θ -scan. This result indicates that the β -FeSi₂ films were epitaxially created on Si(111) substrates without polycrystalline structures.

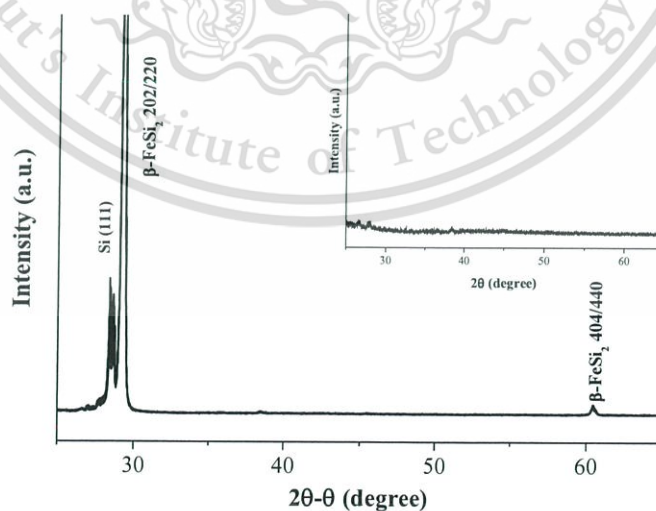


Figure 4.1 XRD pattern for as-produced β -FeSi₂ films on Si(111) substrates measured in 2θ - θ scan. The inset of Figure 4.1 reveals the XRD pattern measured in a 2θ scan with an incidence angle of 4°.

This material is reserved for educational use only, not allowed for commercial use.

Forbidden to modify the content, and cite the document when use.

For measurement of the pole figure pattern, a specific crystallographic plane of 2θ - θ scan should be fixed, which determines the Miller indices of the films. According to the acquired XRD pattern, the β -FeSi₂ 202/220 peak was close to the strong peak of the Si(111) plane. Namely, the acquired pole figure pattern, which was measured in this plane, might present the pole figure of the β -FeSi₂ 202/220 peak with interaction from the Si(111) substrate plane. Consequently, the diffraction peak of β -FeSi₂ 404/440 was chosen as the main scanning plane in this pole figure measurement. Based on the measurement procedure, the pole figure was performed by varying two geometrical parameters, such as the tilt angle (Ψ) from β -FeSi₂ film surface normal direction and the rotation angle (ϕ) around the surface of the films in the normal direction. Figure 4.2 presents the acquired pole figure pattern concerning the peak of β -FeSi₂ 404/440 for the β -FeSi₂ films formed on Si(111) wafers. This pole figure pattern measurement was carried out by employing an XRD apparatus (RINT2000/PC) at Kyushu University. This result demonstrates the occurrence of 3 kinds of epitaxial variants. The rotation angle was 120 degrees from each other [3].

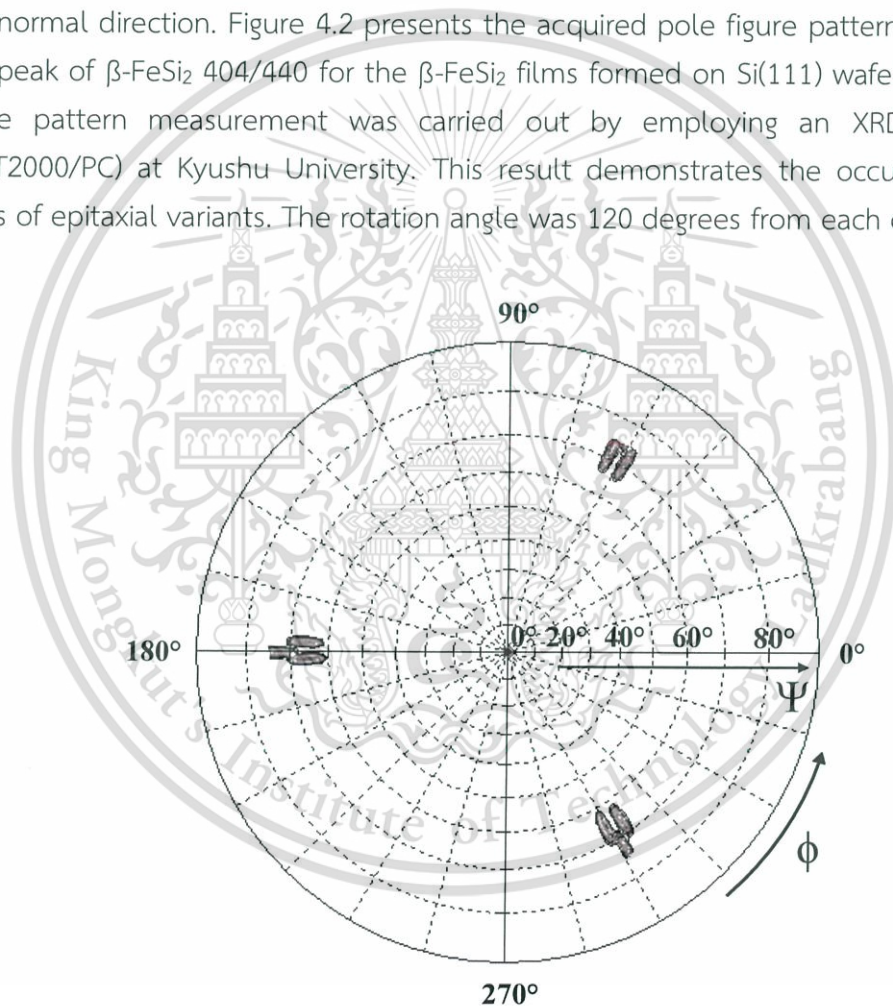


Figure 4.2 Pole-figure pattern of as-produced β -FeSi₂ films on Si(111) substrates.

4.1.2 Raman spectra of as-produced β -FeSi₂ films

Figure 4.3 displays the typical Raman spectra of the as-produced β -FeSi₂ films created on a p-type Si(111) via FTDCS at substrate temperature of 600 °C. Two distinct peaks at ~ 194 cm⁻¹ and ~ 247 cm⁻¹ appeared from the acquired Raman line in a range from 150 to 300 cm⁻¹. In particular, the β -FeSi₂ characteristic peaks were located at ~ 191 cm⁻¹ and ~ 244 cm⁻¹ [58-61]. This result confirmed the creation of β phase in our as-produced FeSi₂ films. The observation of the β -phase for the as-produced FeSi₂ films is in agreement with the results reported by other research groups [59]. Basically, the Raman lines at ~ 194 and ~ 248 cm⁻¹ are predominated by the motion of Fe atoms. The line at ~ 194 cm⁻¹ is associated with angular motions, while the line at ~ 248 cm⁻¹ is associated with the radial motion of Fe atoms [62].

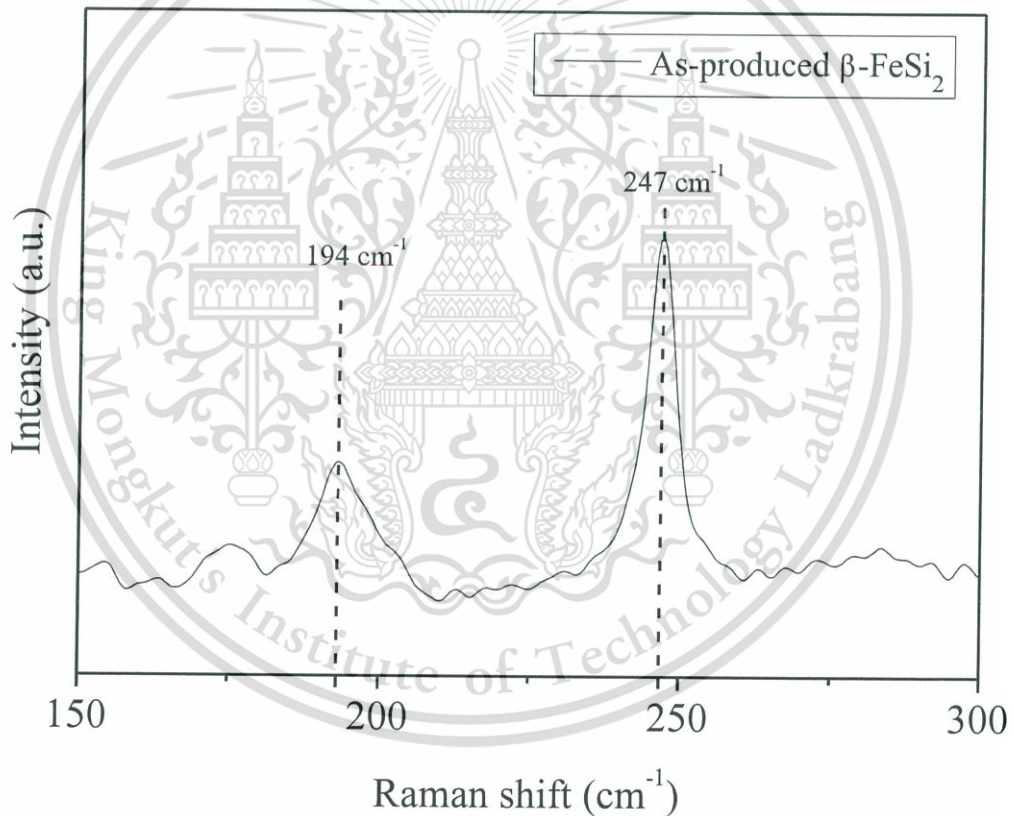


Figure 4.3 Raman lines of as-produced β -FeSi₂ films formed by FTDCS method.

4.1.3 FESEM image of as-produced β -FeSi₂ films

Figure 4.4 presents a FESEM micrograph at 50k magnitude showing a plain surface view of the produced β -FeSi₂ film. It was observed that a large number of crystallites with small sizes covered the film surface. Further, the produced β -FeSi₂ films contained many grain boundaries and a porous area that existed at the edge of the grain boundary of the films.



Figure 4.4 FESEM image in plane surface view of β -FeSi₂ films with 50K of magnitude.

4.1.4 AFM image of as-produced β -FeSi₂ films

An AFM image of the as-created β -FeSi₂ films is illustrated in Figure 4.5. The scanning result, in non-contact mode, demonstrated the rather smooth surface of the as-created β -FeSi₂ films. The estimated root mean square (rms) roughness of the film surface was 2.02 nm. Some pinholes were observable within the scanning area, which conformed to FESEM surface imagery. This can be represented by the fact that, in the production process of β -FeSi₂ films by utilization of FTDCS, the Si substrate is located on a substrate holder far away from the plasma that was created by sputtering [4,9]. Besides, the temperature of the produced β -FeSi₂ film surface did not increase as a result of the Si substrate being positioned far from the plasma region. From this situation, the produced β -FeSi₂ film surface suffered minimal damage from the destruction of plasma [4,9].

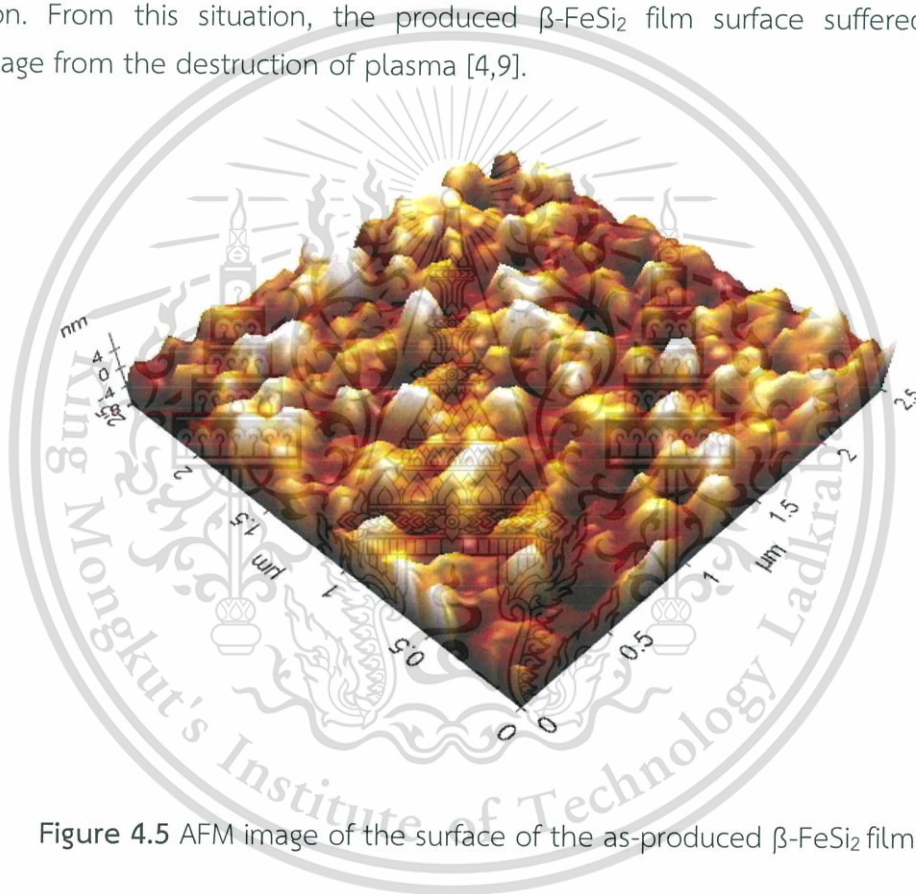


Figure 4.5 AFM image of the surface of the as-produced β -FeSi₂ films.

4.1.5 Wettability of the as-produced β -FeSi₂ films

Figure 4.6 presents an image of the measured contact angle between the surface of the as-created β -FeSi₂ films and water droplets. The average value of the measured contact angle was 98.7° (99.0° and 98.4° for the left and right sides of contact angle, respectively). From the acquired results, the as-created β -FeSi₂ film surface exhibited hydrophobic behavior. Commonly, a hydrophobic surface is labeled as having contact angles in the angle range of $90^\circ < \theta < 150^\circ$ [63,64]. Based on the obtained FESEM image, the as-created β -FeSi₂ film surface has an occurrence of porous territory. This can be explained by the wetting model of Cassie-Baxter, which describes the wetting phenomena of a porous area underneath liquid drops. The porous area is an act to the air pocket, where air can infiltrate into the grooves and support the lifting of dripped liquid, resulting in a higher contact angle than for a flat surface [51,65,66].



Figure 4.6 Contact angle between the water droplet and surface of the as-produced β -FeSi₂ films.

4.2 The physical properties of unannealed and annealed β -FeSi₂ films

4.2.1 Raman spectra of unannealed and annealed β -FeSi₂ films

Figure 4.7 displays the Raman spectra for the as-produced and annealed β -FeSi₂ films under annealing temperatures of 200, 400, and 600 °C. The spectra of these annealed samples showed two typical peaks for the β -FeSi₂ films. The peaks of the Raman lines for all annealed samples were centered at the position approximately of 194 and 247 cm⁻¹, which is the same position as the unannealed β -FeSi₂ films. The obtained results demonstrated that at annealing temperatures of 200, 400, and 600 °C also has a β -phase same as the Raman spectra of the as-produced β -FeSi₂ films.

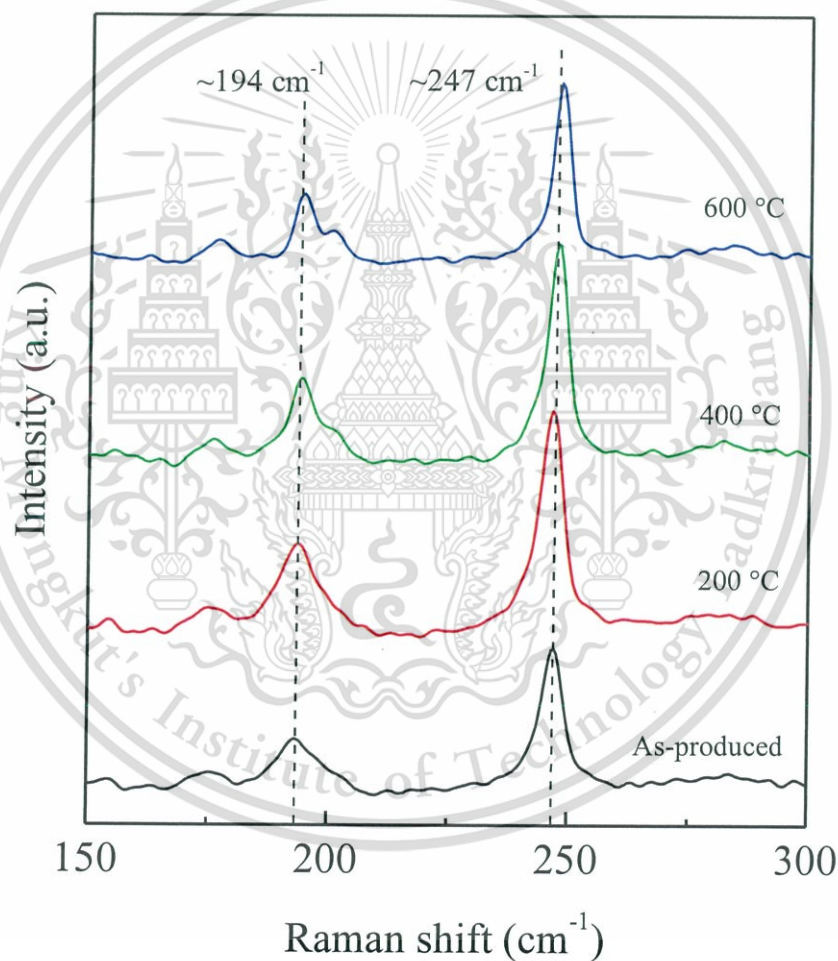


Figure 4.7 Typical Raman spectra for β -FeSi₂ films without annealing and at different annealing temperatures.

4.2.2 FESEM of as-produced and annealed β -FeSi₂ films

Figure 4.8 presents FESEM images in plain surface view of the as-produced β -FeSi₂ films and after annealing at 200, 400, and 600 °C. A large amount of crystallites with small sizes was observed from the FESEM image of the as-produced β -FeSi₂ films. In addition, the unannealed β -FeSi₂ film surface contained many grain boundaries and a porous zone. It was found that the film surface did not change significantly by annealing at our temperature conditions.

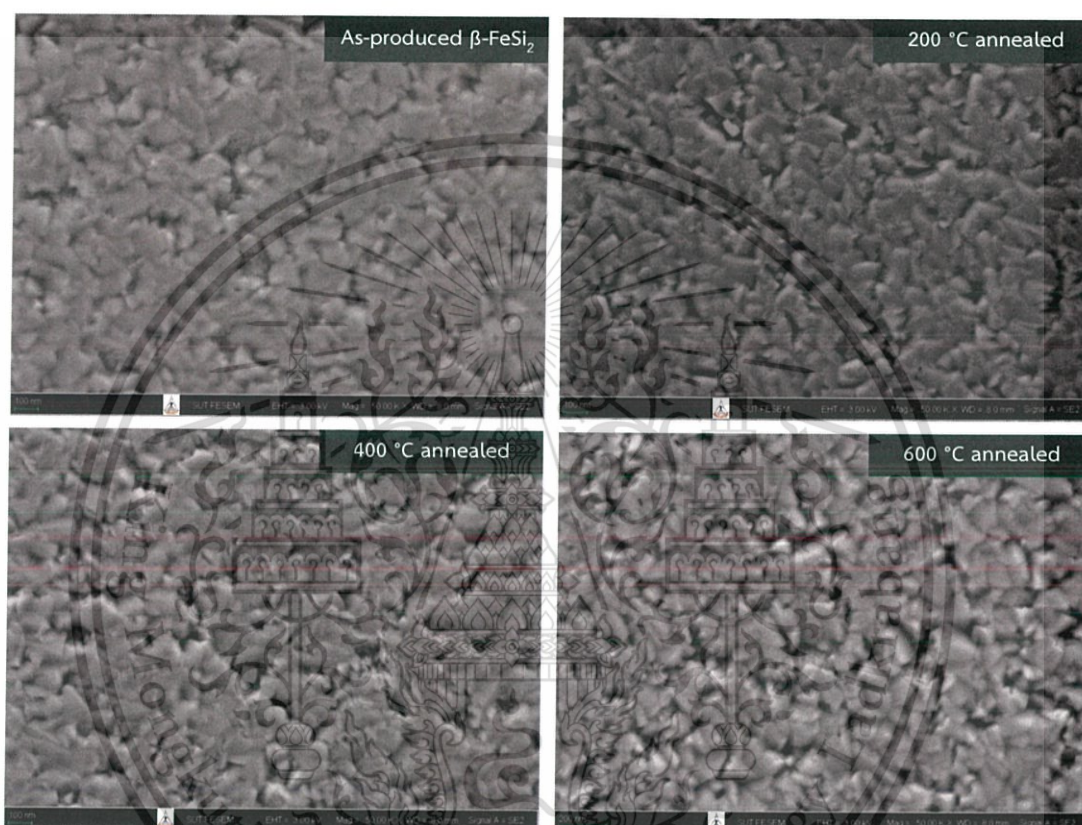


Figure 4.8 Plain-view FESEM micrographs for the as-produced β -FeSi₂ films at and after annealing at 200, 400, and 600 °C.

4.2.3 AFM images of unannealed and annealed β -FeSi₂ films

Figure 4.9 presents the AFM images of β -FeSi₂ films before and after annealing at different temperatures (200, 400, and 600 °C). In the case of non-annealing β -FeSi₂ films, the rms roughness was 2.02 nm and contained pinholes over the film surface. After annealing at 200, 400, and 600 °C, the obtained values were 2.48, 2.30 and 2.33 nm, respectively. The results demonstrated that the roughness of the as-produced β -FeSi₂ film surface changed slightly due to annealing.

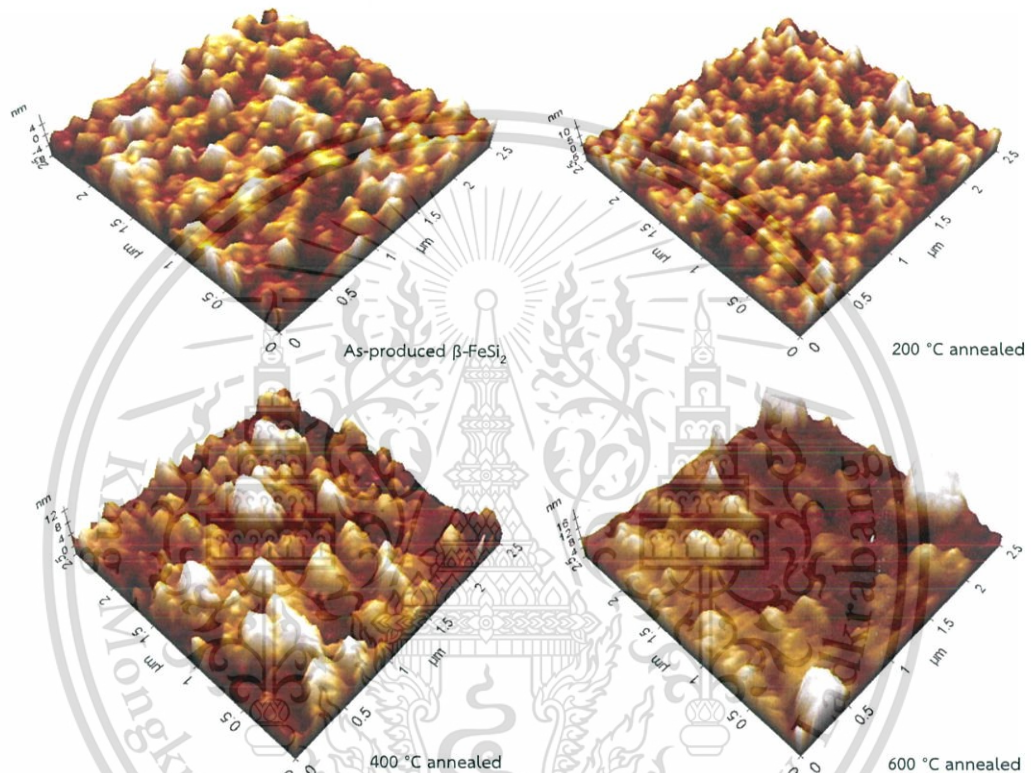


Figure 4.9 AFM images of the β -FeSi₂ films in the case of non-annealing and annealing under various temperatures (200, 400, and 600 °C).

4.2.4 Wettability of as-produced and annealed β -FeSi₂ film surface

The measured contact angles for unannealed β -FeSi₂ films and after annealing at 200, 400, and 600 °C are displayed in Fig 4.10. For unannealed β -FeSi₂ films, the surface of the β -FeSi₂ layer exhibited an average contact angle value of 98.7°. It was found that the average contact angle decreased after the films were annealed. By annealing at 200 °C, the average contact angle value was 91.6°. Based on these results, a hydrophobic contact angle in a range of $90^\circ < \theta < 150^\circ$ [63,64] was recorded for β -FeSi₂ films without annealing and after annealing at 200 °C. The surface of the films showed contact angle values of 88.85° and 82.15° under annealing at 400 and 600 °C, respectively. This result indicated that the film surface after annealing at 400 and 600 °C exhibited hydrophilic behavior with a contact angle in a range of $10^\circ < \theta < 90^\circ$ [63,64]. From this, the surfaces of the film refer to change in the Wenzel model because there is low surface hydrophobicity to save the Cassie–Baxter state. Namely, the larger contact area between the film surface and the drop, due to the porous area between the grain boundaries, is permeated with water. The wettability of the β -FeSi₂ films was decreased same as the annealed results from other research group [56].

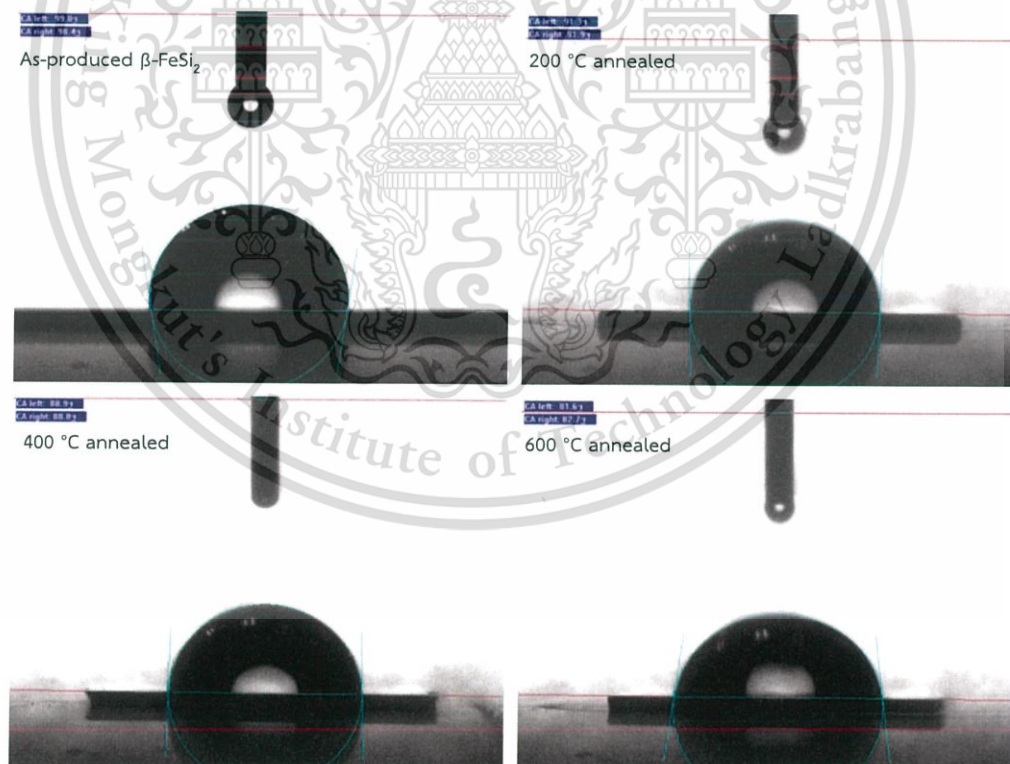


Figure 4.10 Images of contact angles for the as-produced β -FeSi₂ films and β -FeSi₂ films annealed at 200, 400, and 600 °C.

4.3 Physical properties of as-produced NC-FeSi₂ films

4.3.1 XRD pattern of as-produced NC-FeSi₂ films

Figure 4.11 depicts the obtained XRD patterns for the NC-FeSi₂ films formed by FTDCS in comparison with those of the NC-FeSi₂ films formed by PLD. This measurement was carried out with an XRD apparatus (RINT2000/PC) at Kyushu University utilizing the grazing incidence method (2 θ scan) at a fixed incidence angle of 4°. It was clear that these XRD patterns exhibited a broad peak in the range of 40-50°. This can be described by the superposition of several diffraction peaks in β -FeSi₂. The researchers observed that the peak intensity of the NC-FeSi₂ films formed by FTDCS was slightly enhanced when compared to that of the NC-FeSi₂ films formed utilizing PLD [11]. The crystallite size was estimated from the peak of the XRD pattern by using the Scherrer equation, which is expressed as follows [67-69]:

$$D = \frac{0.94\lambda}{\beta \cos \theta} \quad (3.1)$$

where λ is the X-ray wavelength ($\lambda = 1.542 \text{ \AA}$) (CuK α), β is the full width at half maximum (FWHM) in the radian and θ is the diffraction angle. From estimation using the Scherrer equation, the grain sizes of the NC-FeSi₂ films formed by FTDCS and PLD were 5.03 nm and 3.17 nm, respectively. This revealed that the diameters of the crystallite for the NC-FeSi₂ films formed by the utilization of FTDCS were slightly larger than those of the NC-FeSi₂ films formed by PLD.

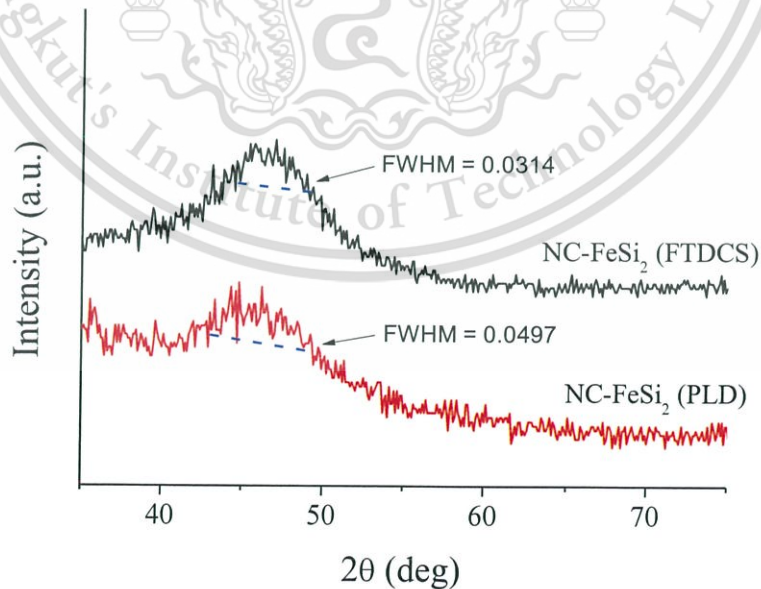


Figure 4.11 XRD patterns of the as-produced NC-FeSi₂ films formed by means of FTDCS and PLD at a fixed incidence angle of 4°.

This material is reserved for educational use only, not allowed for commercial use.

Forbidden to modify the content, and cite the document when use.

4.3.2 Raman spectrum of as-produced NC-FeSi₂ films

Figure 4.12 displays the Raman line of the NC-FeSi₂ layer created on a p-type Si(111) wafer via FTDCS and PLD. From the obtained spectra, two peaks at $\sim 176 \text{ cm}^{-1}$ and $\sim 232 \text{ cm}^{-1}$ appeared in the NC-FeSi₂ samples. Specifically, the β -FeSi₂ characteristic peaks were located at $\sim 191 \text{ cm}^{-1}$ and $\sim 244 \text{ cm}^{-1}$ [58-61]. The peaks of the as-produced NC-FeSi₂ films shifted slightly to have lower phonon energy (red shift) compared to the Raman lines of the β -FeSi₂ characteristic peaks. The red shift of these lines might be due to Co, which is a dominant impurity in the FeSi₂ target and was incorporated from the FeSi₂ target into the films [9]. This red shift of the Raman lines for the FeSi₂ films containing Co was also observed and reported by Fanciulli et al. [61].

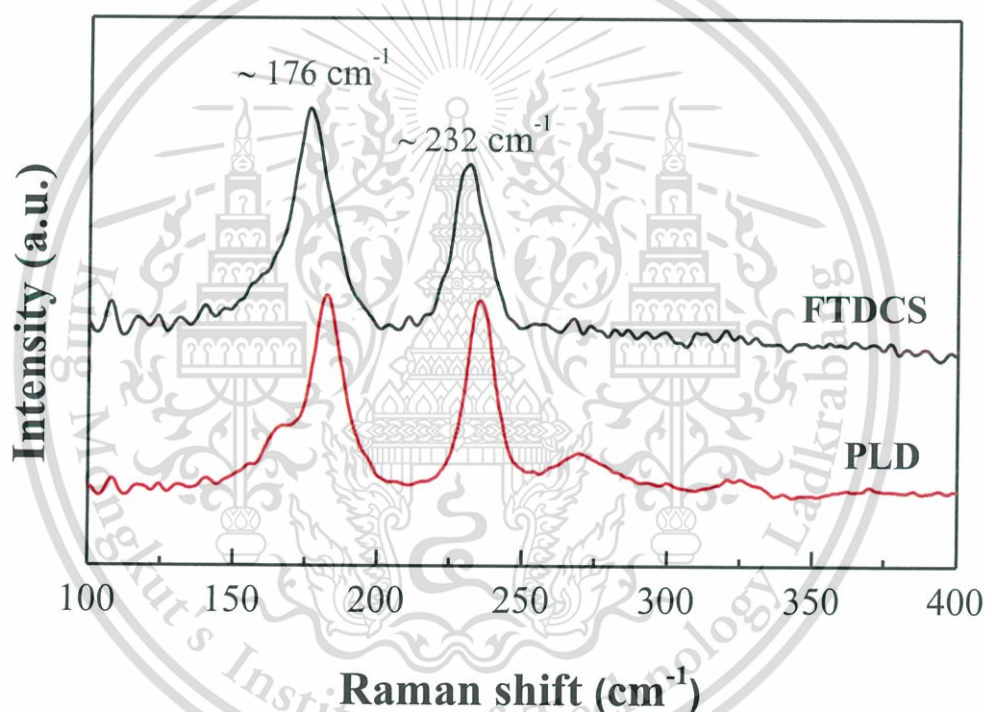


Figure 4.12 Raman lines of as-created NC-FeSi₂ films produced by FTDCS and PLD.

4.3.3 FESEM image of as-produced NC-FeSi₂ films

Figure 4.13(a) and (b) depicts the FESEM images in plain view of as-produced NC-FeSi₂ thin films created by FTDCS and PLD. From the obtained FESEM images in plain view, it was apparent that the unannealed NC-FeSi₂ thin films had a very smooth surface and consisted of numerous small uniform crystallites with diameters of around 5-7 nm. In addition, it could be observed that the surface of NC-FeSi₂ films created by means of PLD was very smooth and continuous with diameters of 3-5 nm. The crystallite diameters of the NC-FeSi₂ films were slightly

larger when compared with those created by PLD. This is because the quenching effect in the PLD process is stronger than that in the FTDCS process [13,16]. Therefore, the NC-FeSi₂ films created by FTDCS were comprised of larger crystallites. This obtained experimental result corresponded to the XRD results for the NC-FeSi₂ films in our previous study [11,16,24].

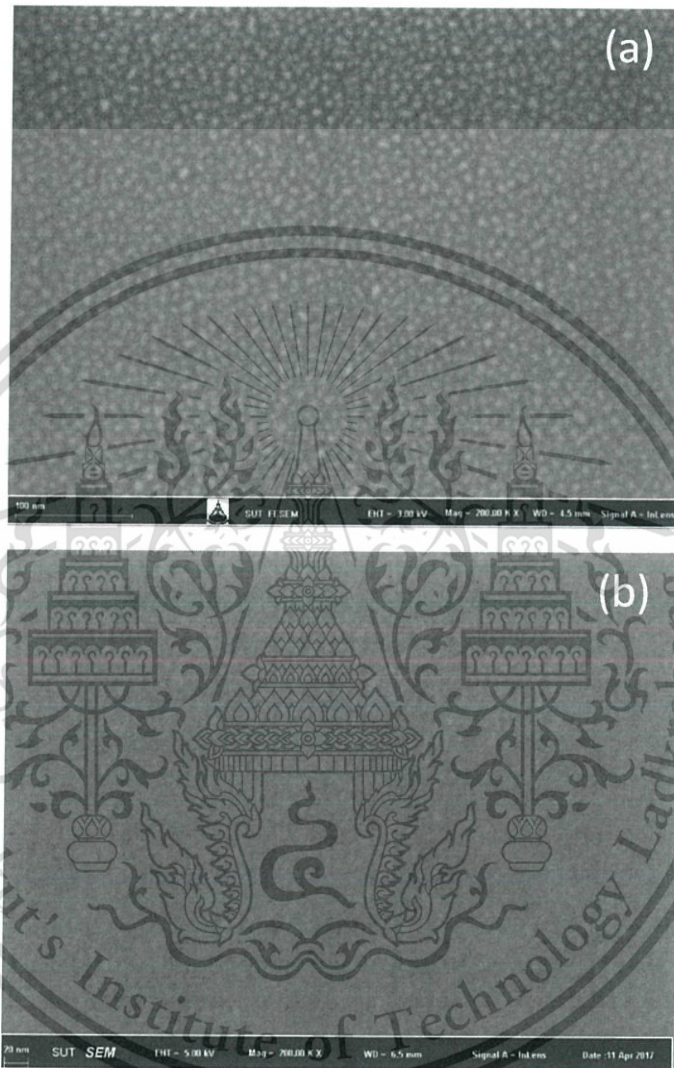


Figure 4.13 FESEM surface of the produced NC-FeSi₂ layer formed via (a) FTDCS and (b) PLD (200,000 magnitude).

Figure 4.14 presents an FESEM image in cross-section view of the as-produced NC-FeSi₂ films. The unannealed NC-FeSi₂ films exhibited a smooth surface. A sharp interface can be seen between the Si wafers and NC-FeSi₂ films.

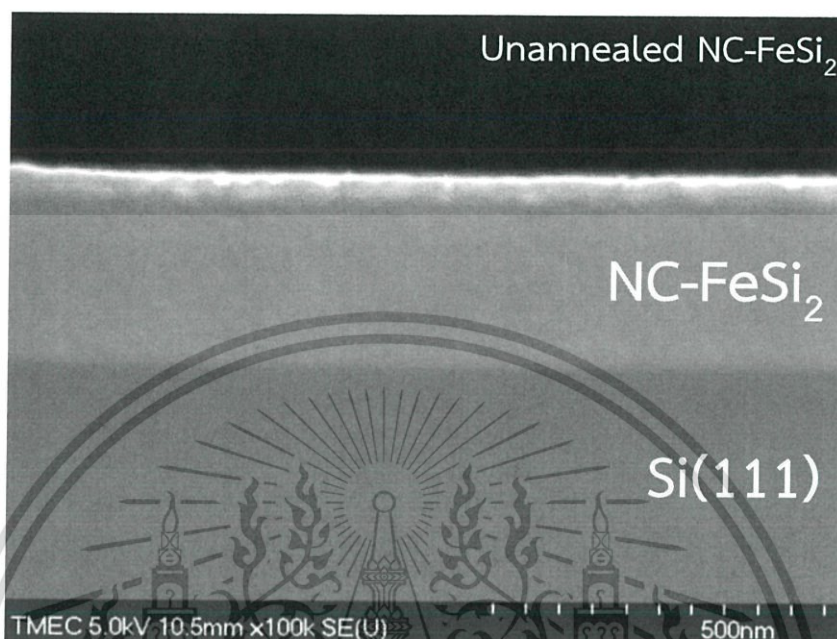


Figure 4.14 Cross-section view of the unannealed Nc-FeSi₂ films formed via FTDCS.

4.3.4 AFM image of as-produced NC-FeSi₂ films

Figure 4.14 presents a three-dimensional AFM image of the as-produced NC-FeSi₂ film surfaces created by FTDCS at room temperature. The surfaces of the as-produced NC-FeSi₂ films were very smooth and continuous. The rms roughness for the surfaces of the as-produced NC-FeSi₂ layer was found to be 0.81 nm. This can be explained by the fact that, in the creation process of NC-FeSi₂ films employing FTDCS at room temperature, the Si substrate is placed on a substrate holder far away from the plasma that was created by the sputtering process. In addition, the film surface temperature during film creation was not increased because the Si substrate was placed far from the plasma [3,4,9]. Based on this situation, damage to the surface of the NC-FeSi₂ films from plasma was very minor. Therefore, the surface of the NC-FeSi₂ films created utilizing FTDCS was relatively smooth.

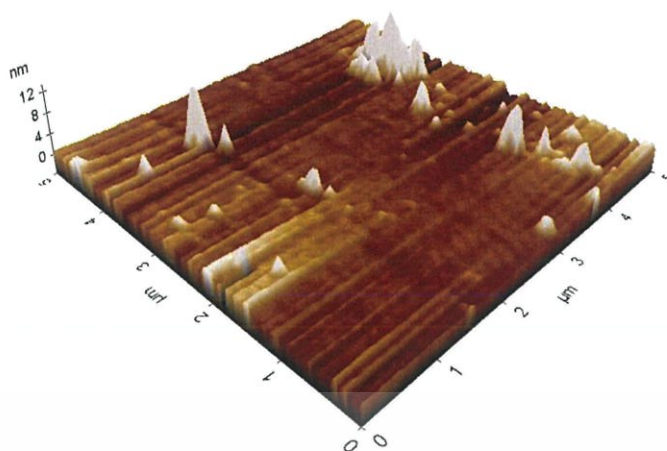


Figure 4.15 Illustration of AFM for the surface of unannealed NC-FeSi₂ films.

4.3.5 Wettability of the surface of as-produced NC-FeSi₂ films

Figure 4.15 presents an image of the measured contact angles for as-produced NC-FeSi₂ films created by FTDCS. For water dropped on the film surface in the case of non-annealing, the average contact angle of NC-FeSi₂ films was 100.1° (100.2° and 100.0° for the left and right sides of contact angle, respectively). The obtained contact angle is in the range of $90^\circ < \theta < 150^\circ$. This experimental result demonstrated that the surface of the NC-FeSi₂ films was hydrophobic. From the FESEM image of the unannealed NC-FeSi₂ films, many porous areas were found among crystallites. This might be explained by the Cassie and Baxter model [57]. Based on this model, the porous area is an act to the air pocket, where air can infiltrate into the grooves and support the lifting of dripped liquid. This results in a higher contact angle than for a flat surface [55,65,66].

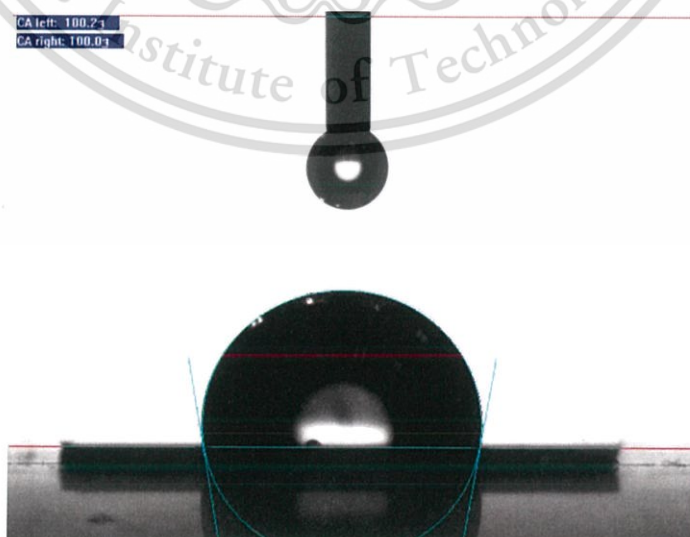


Figure 4.16 Image of water droplet on the surface of the NC-FeSi₂ films.

This material is reserved for educational use only, not allowed for commercial use.

Forbidden to modify the content, and cite the document when use.

4.4 Physical properties of as-created and annealed NC-FeSi₂ films

4.4.1 XRD patterns of as-created and annealed NC-FeSi₂ films

Figure 4.16 depicts XRD patterns for the as-produced NC-FeSi₂ films and annealed NC-FeSi₂ films at 300, 600 and 900 °C. This measurement was performed with a XRD diffractometer (Rigaku, TTRAX III) using the grazing incidence method (2 θ -scan) at an incidence angle of 2°. A broad peak was observed at 2 θ ranging from 40-50°. This might be due to the overlapping of many diffraction peaks of β -FeSi₂. This peak intensity was slightly increased at an annealing temperature of 300 °C. The peak intensity is observed to increase considerably with annealing at 600 and 900 °C. Ordinarily, peak intensity is related to crystallinity. Thus, higher peak intensity for annealing at 900 °C generates higher crystallinity [70]. Additionally, many preferred orientations appeared on the XRD pattern of NC-FeSi₂ films annealed at 600 °C and 900 °C. According to the obtained result, the appearance of many preferred orientations and the enhancement of film crystallinity were observed as annealing temperature was increased to 600 °C. This was potentially likely, as the atoms would be capable of gaining higher diffusion activation energy when the NC-FeSi₂ films were annealed at higher temperatures. This would allow the atoms with a lower surface energy to move to an energetically favorable place in the lattice of the crystal. Then, the crystallites grow to the preferred direction with the energy provided at the higher temperature. For this reason, film crystallinity is improved [71].

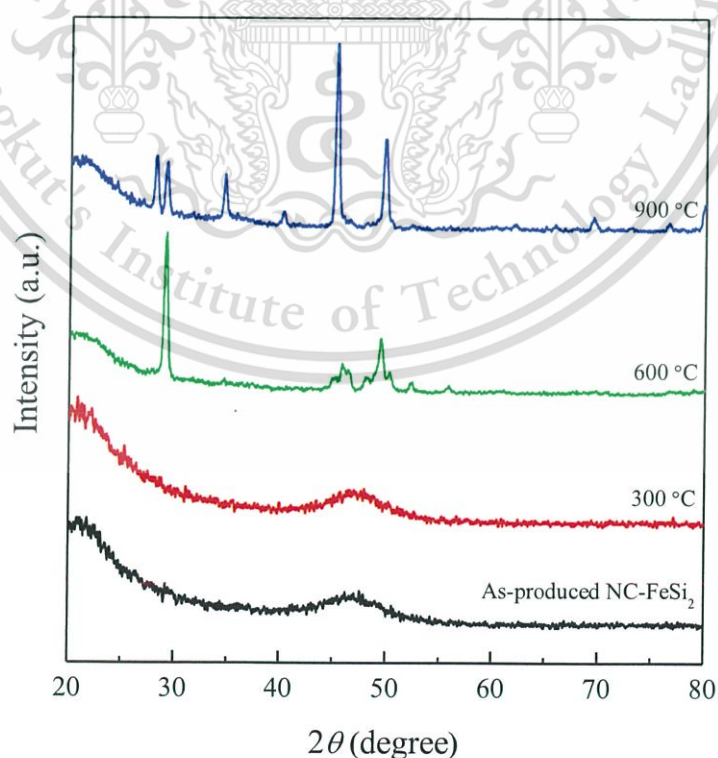


Figure 4.17 XRD patterns of the as-produced and annealed NC-FeSi₂ films.
This material is reserved for educational use only, not allowed for commercial use.

4.4.2 Raman spectra of the as-created and annealed NC-FeSi₂ films

Figure 4.18 displays the Raman lines for the as-created and annealed NC-FeSi₂ layers created via FTDCS method. From the obtained spectrum of as-produced NC-FeSi₂ films, two intensive peaks were centered at positions of approximately 176 cm⁻¹ and 232 cm⁻¹. The Raman lines that appeared for all annealed NC-FeSi₂ samples were identified in the same position as the non-annealing condition with no-displacement in the peak position.

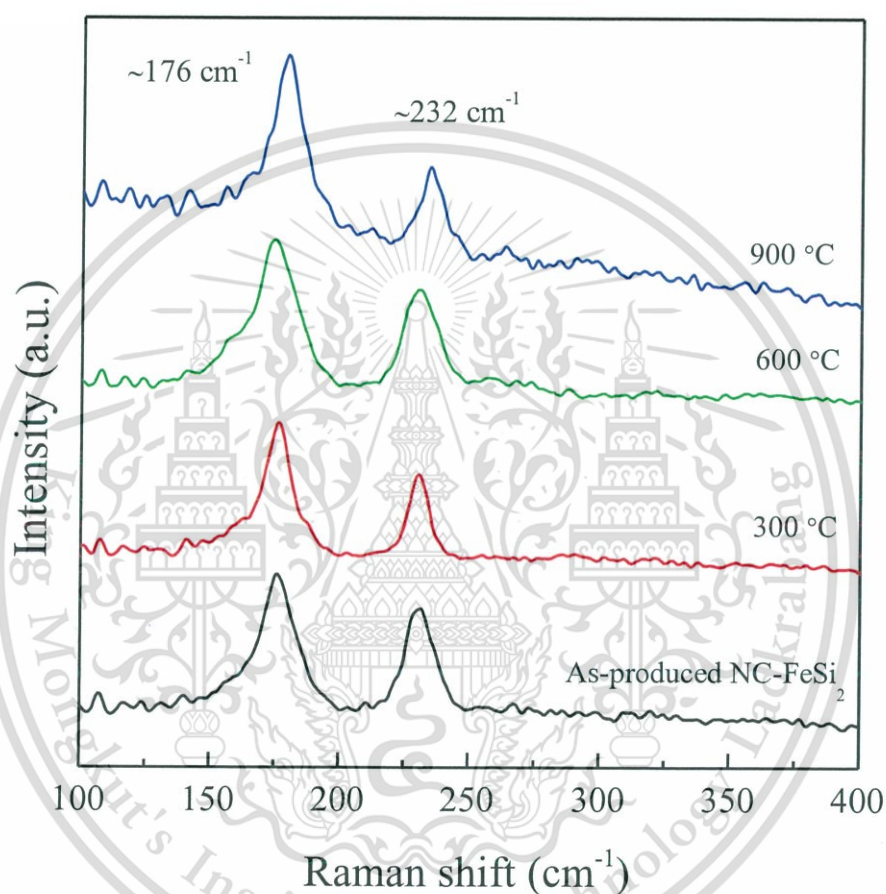


Figure 4.18 Raman spectra of annealed NC-FeSi₂ films under various annealing temperatures in comparison with as-produced NC-FeSi₂ films.

4.4.3 FESEM images of the as-produced and annealed NC-FeSi₂ films

Figure 4.17 depicts FESEM images in plain view of NC-FeSi₂ films created by FTDCS in the case of non-annealing and annealing at temperatures of 300, 600, and 900 °C. From the obtained FESEM images, it was apparent that the unannealed NC-FeSi₂ films had a very smooth surface and consisted of numerous small uniform crystallites with diameters of around 5-7 nm. At an annealing temperature of 300 °C, the small uniform crystallites in NC-FeSi₂ films were merged into nanocrystalline clusters. The spaces between the merged nanocrystalline clusters increased in comparison with the spaces between the crystallites of the unannealed NC-FeSi₂ films. When the NC-FeSi₂ films were annealed at 600 °C, the uniform crystallites were occasionally clustered. They were completely clustered and became several larger clusters when the annealing temperature was increased to 900 °C.

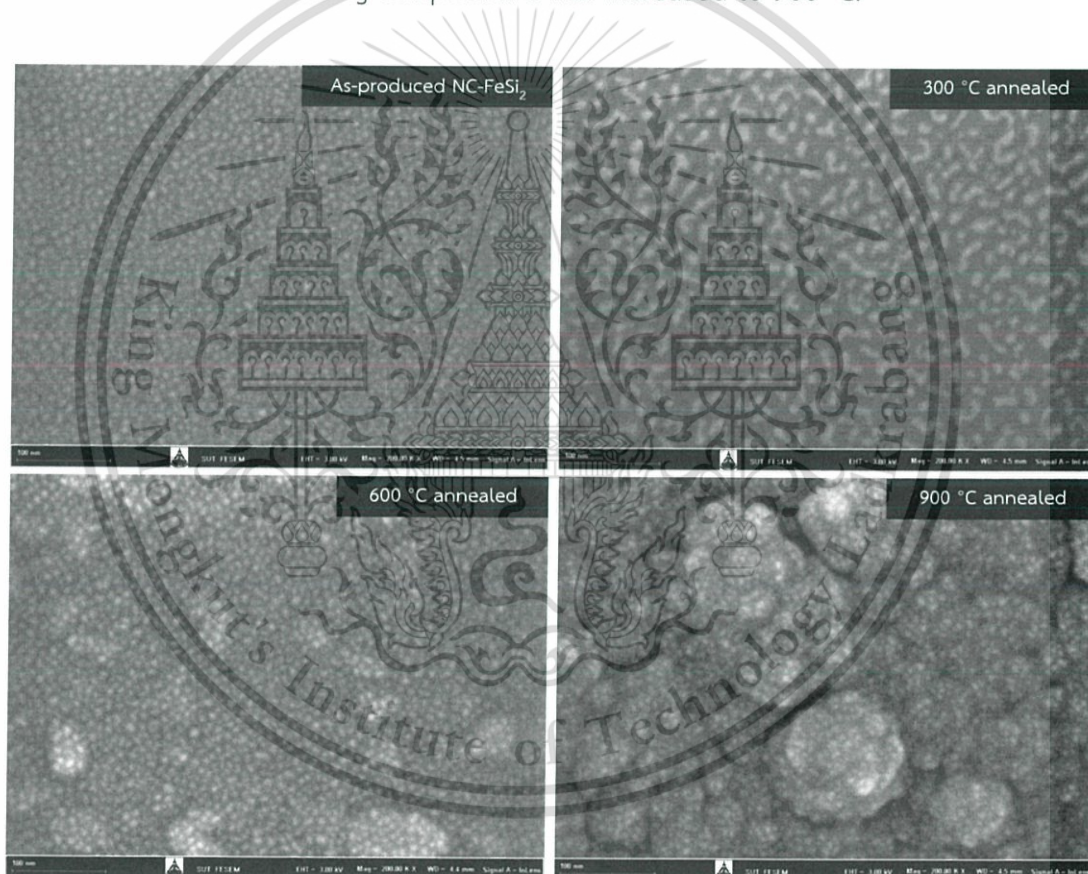


Figure 4.19 FESEM images in plane surface view of as-created NC-FeSi₂ films and after annealing at temperatures of 300 °C, 600 °C, and 900 °C.

The cross-section view for as-produced NC-FeSi₂ films and after annealing at 300, 600, and 900 °C of annealing temperature is shown in Figure 4.20. From observation of film interface, all the NC-FeSi₂ films showed a keen interface and non-fragility along the line. The film surface of as-produced and annealed NC-FeSi₂, at 300 and 600 °C, exhibited a smooth surface. However, the surface of the NC-FeSi₂ films annealed at 900 °C was rough owing to the formation of many large clusters of clustered crystalline structures.

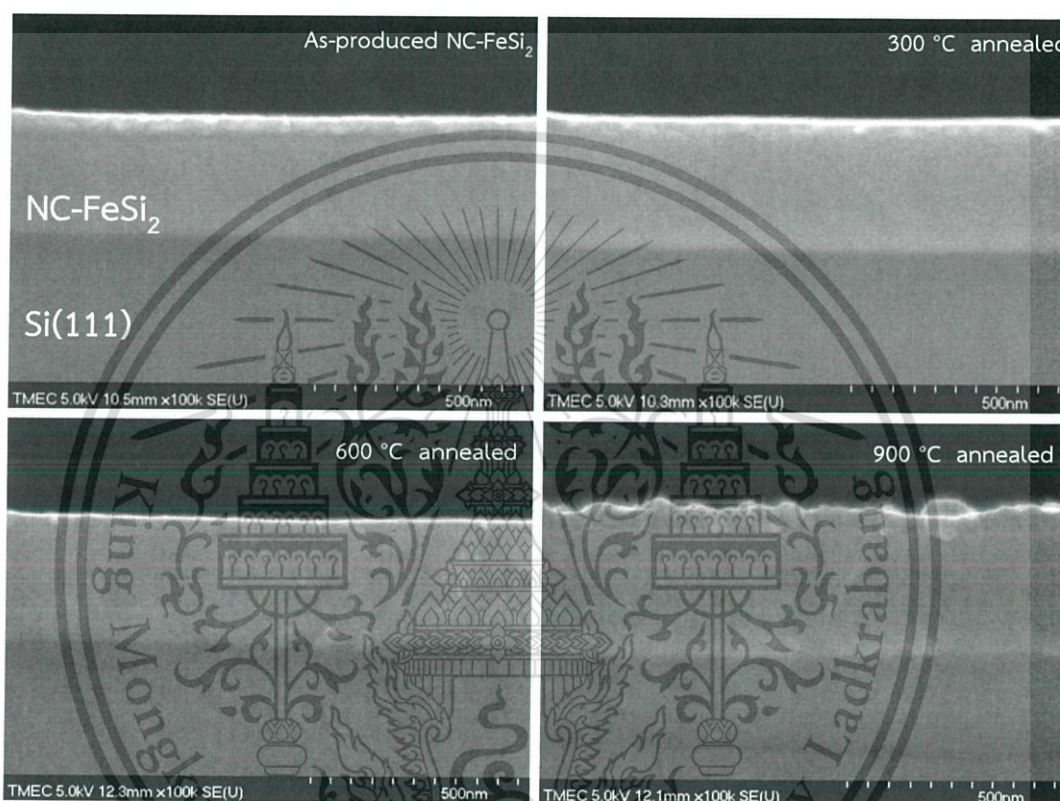


Figure 4.20 Crosssectional view of as-created NC-FeSi₂ films and after annealing at temperatures of 300 °C, 600 °C and 900 °C.

4.4.4 AFM images of as-produced and annealed NC-FeSi₂ films

Figure 4.21 shows the surface of the as-produced and annealed NC-FeSi₂ films. It can be observed that the surfaces of the unannealed NC-FeSi₂ films were very smooth. The rms roughness of the unannealed NC-FeSi₂ film surface was about 0.81 nm. Increasing the annealing temperatures to 300 and 600 °C caused the rms roughness to gradually increase. The rms roughness values were 1.30 and 1.71 at annealing temperatures of 300 and 600 °C, respectively. When the annealing temperature was increased to 900 °C, the surface of the NC-FeSi₂ films was rougher than those at other temperatures. According to the estimation from the AFM image, the rms roughness was increased to 10.78 nm. The results from FESEM showed that

numerous small crystalline clusters formed and became big clusters under an annealing temperature of 900 °C. In addition, pinholes appeared on the film surface. Based on these causes, the surface of the NC-FeSi₂ films annealed at 900 °C should be rougher.

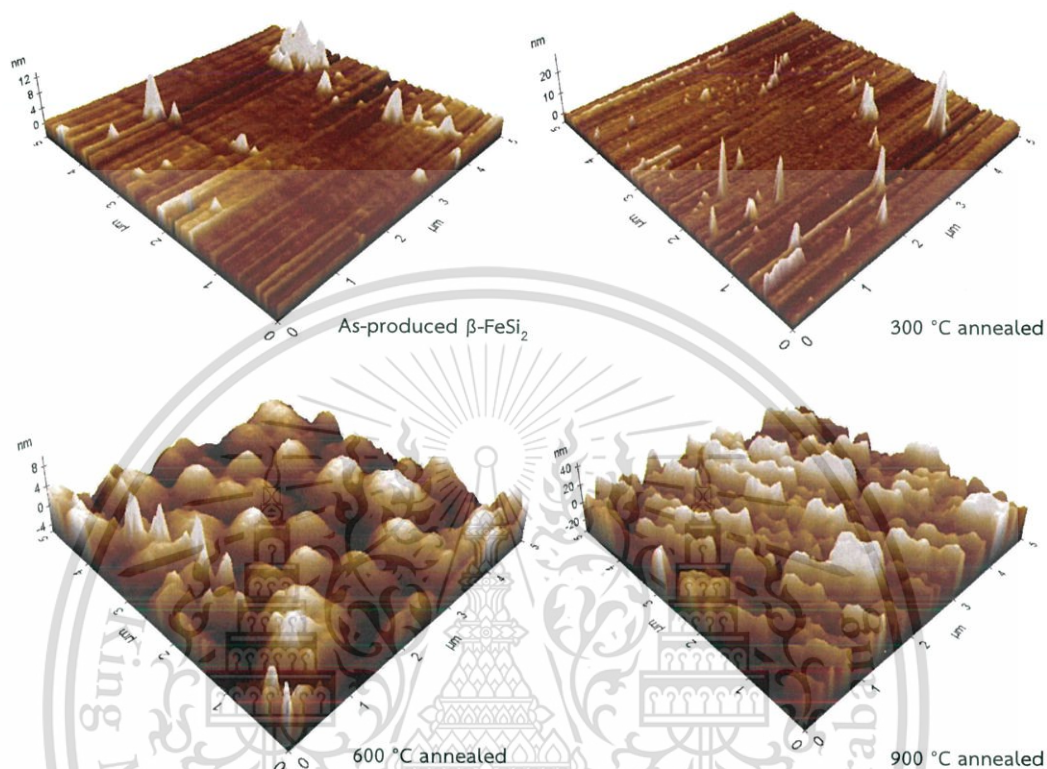


Figure 4.21 AFM images of the NC-FeSi₂ film surfaces in case of non-annealing and annealing temperature of 300, 600, and 900 °C.

4.4.5 Wettability of the surface of as-created and annealed NC-FeSi₂ films

Figure 4.22 presents images of the measured contact angles for as-created and annealed NC-FeSi₂ films (300, 600, and 900 °C). For water dropped on the as-produced NC-FeSi₂ film surface, the average contact angle was 100.1°. The acquired contact angle was in the range of $90^\circ < \theta < 150^\circ$. This experimental result revealed that the surface of the NC-FeSi₂ films was hydrophobic. When the NC-FeSi₂ thin films were annealed at a temperature of 300 °C, the average contact angle was increased to 106.2°. According to the acquired surface morphology from the FESEM image of the NC-FeSi₂ films under annealing at 300 °C, the average size of nanocrystalline clusters generated from the merged small crystallites and space among nanocrystalline clusters were increased in comparison with those of unannealed NC-FeSi₂ films. This behavior can be explained by the Cassie and Baxter model, in which air trapped between the nanocrystalline clusters increases the air-

This material is reserved for educational use only, not allowed for commercial use.

liquid contact area [57]. NC-FeSi₂ films under annealing at 300 °C should form a higher contact angle as a result. After the annealing temperatures were increased to 600 °C and 900 °C, the average contact angles were decreased. The average contact angle of the annealed NC-FeSi₂ films at annealing temperatures of 600 and 900 °C were 71.2° and 67.0°, respectively. This behavior of NC-FeSi₂ thin film surfaces implies the transition to the Wenzel model because there is inadequate surface hydrophobicity to maintain the Cassie–Baxter condition. Namely, the gaps that exist between the nanostructures are filled with water because, at high annealing temperatures, a water-solid interface becomes more favorable than an air-solid interface. Thus, the bottom of water droplets had conformal contact with the solid surface. This conformal contact between water and solid increases the water-solid interfacial force on the surface, which causes a decrease in contact angle [72].

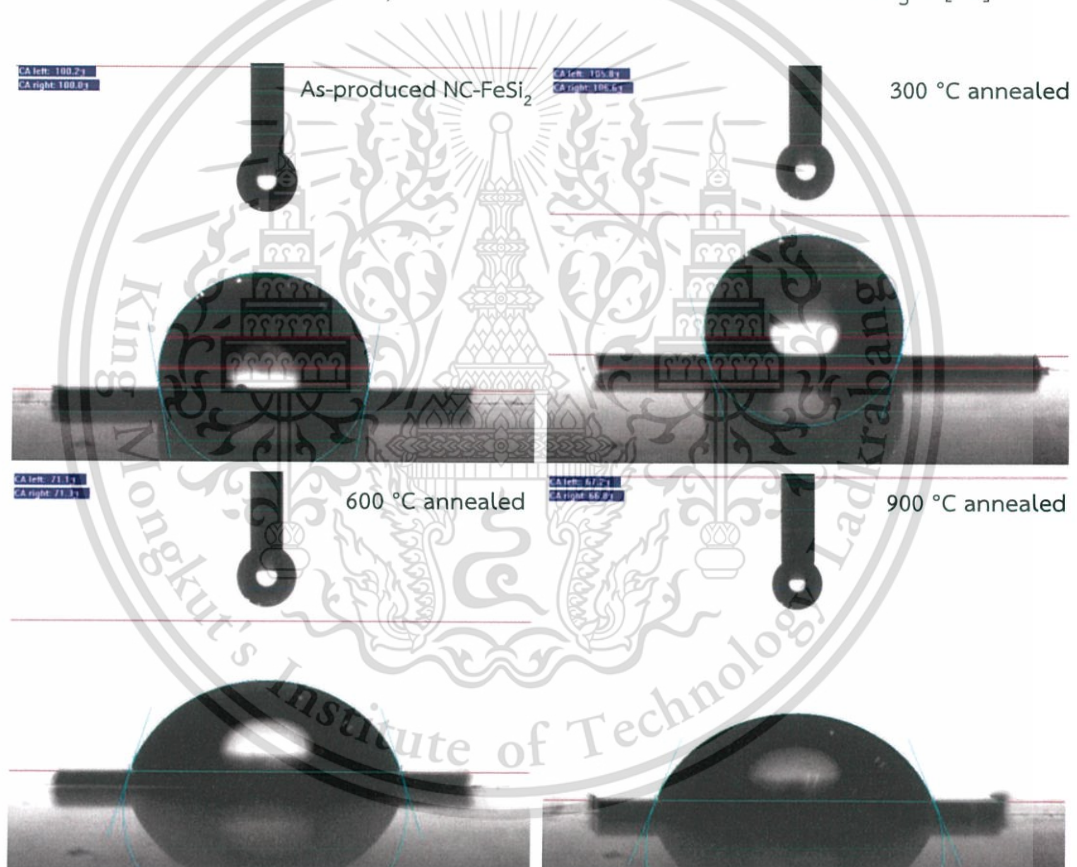


Figure 4.22 Contact angles of as-produced and annealed NC-FeSi₂ films (300, 600 and 900 °C).

Chapter 5

Summary and Suggestions for Future Work

This chapter summarizes the experimental results gained from the research and provides suggestions for related research work requiring further study in the future.

5.1 Summary

In this research, β -FeSi₂ films were epitaxially formed on Si(111) wafer substrates via utilization of FTDCS. The sputtering pressure was set at 1.33×10^{-1} Pa and the substrate temperature was maintained at 600 °C. After formation, the as-formed β -FeSi₂ films were transferred to the annealing system and annealed for two hours in a vacuum at 200, 400 and 600 °C. The peaks of Raman line were located at the positions of 194 and 247 cm⁻¹, which affirmed the formation of the β phase for as-produced FeSi₂ films. These peak positions were not changed significantly by annealing. The FESEM image of the as-formed β -FeSi₂ films exhibits a large amount of crystallites, including many grain boundaries and a porous area. After annealing, the FESEM images exhibited similar surface morphology. The rms roughness of the as-formed β -FeSi₂ films was 2.02 nm, which changed slightly after annealing. The average contact angle between the water droplet and as-formed β -FeSi₂ film surface was found to be 98.70°. This result showed that the surface of the β -FeSi₂ films was hydrophobic. The average contact angle value decreased to 82.15° at an annealing temperature of 600 °C. The acquired experimental results revealed that annealing affected the wettability properties of as-formed β -FeSi₂ films, whereas surface morphology was not greatly affected.

Utilizing FTDCS, NC-FeSi₂ films were created at room temperature. The NC-FeSi₂ films were annealed at temperatures of 300, 600, and 900 °C under high vacuum for 2 hours. The XRD results of the as-created NC-FeSi₂ and after annealing at 300 °C show a broad peak at 2θ ranging from 40 to 50°. The NC-FeSi₂ films annealed at 600 and 900 °C consisted of several preferred orientations and showed improved crystallinity. The peaks of Raman lines for unannealed and annealed NC-FeSi₂ films were observed with no shifting of the peak position at approximately 176 and 232 cm⁻¹. Based on FESEM micrographs in plane view, the unannealed NC-FeSi₂ films were composed of a large amount of small uniform crystallites with diameters of 6-7 nm. At an annealing temperature of 300 °C, the small uniform crystallites were merged and formed into small nanocrystalline clusters. At annealing

This material is reserved for educational use only, not allowed for commercial use.

temperatures higher than 300 °C, the small uniform crystallites were clustered and became large clusters. From an AFM micrograph, the unannealed NC-FeSi₂ films showed a very smooth surface with a rms roughness of 0.81 nm, which was increased by annealing. The unannealed NC-FeSi₂ films exhibited an average contact angle of 100.0°, which was higher than 90°. At an annealing temperature of 300 °C, the film surface exhibited the highest contact angle of 106.2°. The average contact angles were decreased at annealing temperatures higher than 300 °C. The experimental results demonstrated that the annealing temperature influenced the surface morphology, as well as the structural and wettability properties of NC-FeSi₂ films.

5.2 Suggestions

The current research provides the following suggestions for related work in the future:

- 1) The surface morphology and wettability of the β -FeSi₂ and NC-FeSi₂ films should be studied under different annealing atmospheres, such as H₂, O₂, N₂, and Ar.
- 2) The surface morphology and wettability of the β -FeSi₂ and NC-FeSi₂ films should be studied with different fabrication methods, such as PLD and conventional magnetron sputtering.
- 3) The effects of doping of elements on β -FeSi₂ and NC-FeSi₂ films on the surface morphology and wettability of the films should be examined.
- 4) The influence of annealing temperature on the optical and electrical properties of β -FeSi₂ and NC-FeSi₂ films should be investigated.
- 5) The effect of plasma etching on the surface and wetting properties of β -FeSi₂ and NC-FeSi₂ films should be studied

References

- [1] Leong, D. Harry, M. Reeson, K.J. and Homewood, K.P. 1997. "A silicon/iron-disilicide light-emitting diode operating at a wavelength of 1.5 μm ." *Nature*. 387(6634) : 686-688.
- [2] Sunohara, T. Kobayashi, K. and Suemasu, T. 2006. "Epitaxial growth and characterization of Si-based light-emitting Si/ β -FeSi₂ film/Si double heterostructures on Si (001) substrates by molecular beam epitaxy." *Thin Solid Films*. 508(1-2) : 371-375.
- [3] Shaban, M. Nomoto, K. Izumi, S. and Yoshitake, T. 2009. "Characterization of near-infrared n-type β -FeSi₂/p-type Si heterojunction photodiodes at room temperature." *Applied Physics Letters*. 94(22) : 222113-1-22211-3.
- [4] Promros, N. Baba, R. Takahara, M. Mostafa, T.M. Sittimart, P. Shaban, M. and Yoshitake, T. 2016. "Epitaxial growth of β -FeSi₂ thin films on Si (111) substrates by radio frequency magnetron sputtering and their application to near-infrared photodetection." *Japanese Journal of Applied Physics*. 55(6S2) : 06HC03-1-06HC03-4.
- [5] Shaban, M. Izumi, S. Nomoto, K. and Yoshitake, T. 2009. "n-Type β -FeSi₂/intrinsic-Si/p-type Si heterojunction photodiodes for near-infrared light detection at room temperature." *Applied Physics Letters*. 95(16) : 162102-1-162102-2.
- [6] Promros, N. Yamashita, K. Iwasaki, R. and Yoshitake, T. 2012. "Effects of hydrogen passivation on near-infrared photodetection of n-type β -FeSi₂/p-type Si heterojunction photodiodes." *Japanese Journal of Applied Physics*. 51(10R) : 108006-1-108006-2.
- [7] Bost, M.C. and Mahan, J.E. 1988. "A clarification of the index of refraction of beta-iron disilicide." *Journal of Applied Physics*. 64(4) : 2034-2037.
- [8] Tatar, B. Kutlu, K. and Ürgen, M. 2007. "Synthesis of β -FeSi₂/Si heterojunctions for photovoltaic applications by unbalanced magnetron sputtering." *Thin Solid Films*. 516(1) : 13-16.
- [9] Yoshitake, T. Inokuchi, Y. Yuri, A. and Nagayama K. 2006. "Direct epitaxial growth of semiconducting β -FeSi₂ thin films on Si (111) by facing targets direct-current sputtering." *Applied Physics Letters*. 88(18) : 182104-1-182104-3.

- [10] Izumi, S. Shaban, M. Promros, N. Nomoto, K. and Yoshitake, T. 2013. "Near-infrared photodetection of β -FeSi₂/Si heterojunction photodiodes at low temperatures." *Applied Physics Letters*. 102(3) : 032107-1-032107-4.
- [11] Yoshitake, T. Yatabe, M. Itakura, M. Kuwano, N. Tomokiyo, Y. and Nagayama, K. 2003. "Semiconducting nanocrystalline iron disilicide thin films prepared by pulsed-laser ablation." *Applied Physics Letters*. 83(15) : 3057-3059.
- [12] Promros, N. Yamashita, K. Li, C. Kawai, K. Shaban, M., Okajima, T., and Yoshitake, T. 2012. "n-Type nanocrystalline FeSi₂/intrinsic Si/p-type Si heterojunction photodiodes fabricated by facing-target direct-current sputtering." *Japanese Journal of Applied Physics* 51(2R): 021301-1-021301-4.
- [13] Promros N., Chen L., and Yoshitake T. 2013. "Near-infrared photodetection in n-type nanocrystalline FeSi₂/p-type Si heterojunctions." *Journal of Nanoscience and Nanotechnology* 13(5): 3577-3581.
- [14] Funasaki, S. Promros, N. Iwasaki, R. Takahara, M. Shaban, M. and Yoshitake, T. 2013. "Fabrication of mesa structural n-type nanocrystalline-FeSi₂/p-type Si heterojunction photodiodes by liftoff technique combined with photolithography." *Physica Status Solidi (C)*. 10(12) : 1785-1788.
- [15] Promros, N. Baba, R. Kishimoto, H. Sittimart, P. Hanada, T. Hanada, K. Zkia, A., Shaban, M. and Yoshitake, T. 2016. "Characterization of n-type nanocrystalline iron disilicide/intrinsic ultrananocrystalline diamond/amorphous carbon composite/p-type silicon heterojunctions at low temperatures." *Journal of Nanoelectronics and Optoelectronics*. 11(5) : 579-584.
- [16] Nopparuchikun, A. Promros, N. Sittimart, P. Onsee, P. Duangrawa, A. Teakchaicum, S. Nogami, T. and Yoshitake, T. 2017. "Interface-state density estimation of n-type nanocrystalline FeSi₂/p-type Si heterojunctions fabricated by pulsed laser deposition." *Advances in Natural Sciences: Nanoscience and Nanotechnology*. 8(3) : 035016-1-035016-6.
- [17] Promros, N. Sittimart, P. and Kaenrai, W. 2016. "Investigation of electrical transport properties in heterojunctions comprised of silicon substrate and nanocrystalline iron disilicide films." *International Journal of Nanotechnology*. 13(10-12) : 903-912.
- [18] Sittimart, P. Duangrawa, A. Onsee, P. Teakchaicum, S. Nopparuchikun, A. and Promros, N. 2018. "Interface state density and series resistance of n-type nanocrystalline FeSi₂/p-type Si heterojunctions formed by utilizing facing-target direct-current sputtering." *Journal of Nanoscience and Nanotechnology*. 18(3) : 1841-1846.

- [19] Shaban, M. Kawai, K. Promros, N. and Yoshitake, T. 2010. "n-Type nanocrystalline-FeSi₂ /p-Type Si heterojunction photodiodes prepared at room temperature." *IEEE Electron Device Letters*. 31(12) : 1428-1430.
- [20] Nakamura, Y. Nagadomi, Y. Cho, S.P. Tanaka, N. and Ichikawa, M. 2006. "Formation of ultrahigh density and ultrasmall coherent β -FeSi₂ nanodots on Si (111) substrates using Si and Fe codeposition method." *Journal of Applied Physics*. 100(4) : 044313-1-044313-5
- [21] Takarabe, K. Doi, H. Mori, Y. Fukui, K. Shim, Y. Yamamoto, N. Yoshitake, T., and Nagayama, K. 2006. "Optical properties of nanocrystalline FeSi₂ and the effects of hydrogenation." *Applied Physics Letters*. 88(6) : 061911-1-061911-3.
- [22] Nakamura, Y. Nagadomi, Y. Cho, S.P. Tanaka, N. and Ichikawa, M. 2005. "Formation of strained iron silicide nanodots by Fe deposition on Si nanodots on oxidized Si (111) surfaces." *Physical Review B*. 72(7) : 075404-1-075404-7.
- [23] Grimaldi, M.G. Bongiorno, C. Spinella, C. Grilli, E. Martinelli, L. Migas, D.B. Miglio, L., and Fanciulli, M. 2002. "Luminescence from β -FeSi₂ precipitates in Si. I. Morphology and epitaxial relationship." *Physical Review B*. 66(8) : 085319-1-085319-10.
- [24] Shaban, M. Kondo, H. Nakashima, K. and Yoshitake, T. 2008. "Electrical and photovoltaic properties of n-type nanocrystalline-FeSi₂/p-type Si heterojunctions prepared by facing-targets direct-current sputtering at room temperature." *Japanese Journal of Applied Physics*. 47(7R) : 5420-5422.
- [25] Borisenko, V.E. 2013. *Semiconducting Silicides: Basics, Formation, Properties*. Springer Science & Business Media.
- [26] Chen, L.J. 2004. *Silicide Technology for Integrated Circuits*, The institution of Engineering and Technology: United Kingdom.
- [27] Yang, Z. and Homewood, K.P. 1996. "Effect of annealing temperature on optical and structural properties of ion-beam-synthesized semiconducting FeSi₂ layers." *Journal of Applied Physics*. 79(8) : 4312-4317.
- [28] Shaban, M. Nomoto, K. Nakashima, K. and Yoshitake, T. 2008. "Low-temperature annealing of n-type β -FeSi₂/p-type Si heterojunctions." *Japanese Journal of Applied Physics*. 47(5R) : 3444-3446
- [29] Olk, C.H. Yalisove, S.M. and Doll, G.L. 1995. "Defect-induced absorption-band-edge values in β -FeSi₂." *Physical Review B*. 52(3) : 1692-1698.

- [30] Shaban, M. Nakashima, K. and Yoshitake, T. 2007. "Substrate temperature dependence of photovoltaic properties of β -FeSi₂/Si heterojunctions prepared by facing-target DC sputtering." *Japanese Journal of Applied Physics*. 46(12R) : 7708-7710.
- [31] Hossain, M.Z. Mimura, T. Miura, N. and Uekusa, S.I. 2009. "Surface morphology and luminescence characterization of β -FeSi₂ thin films prepared by pulsed laser deposition." *Applied Surface Science*. 256(4) : 1227-1231.
- [32] Christensen, N.E. 1990. "Electronic structure of β -FeSi₂". *Physical Review B*. 42(11) : 7148-7153.
- [33] Bost, M.C. and Mahan, J.E. 1985. "Optical properties of semiconducting iron disilicide thin films." *Journal of Applied Physics*. 58(7) : 2696-2703.
- [34] Suzuno, M. Murase, S. Koizumi, T. and Suemasu, T. 2008. "Improved Room-Temperature 1.6 μ m Electroluminescence from p-Si/ β -FeSi₂/n-Si Double Heterostructures Light-Emitting Diodes." *Applied physics express*. 1(2) : 021403-1-021403-3.
- [35] Suzuno, M. Koizumi, T. and Suemasu, T. 2009. "p-Si/ β -FeSi₂/n-Si double-heterostructure light-emitting diodes achieving 1.6 μ m electroluminescence of 0.4 mW at room temperature." *Applied physics letters*. 94(21) : 213509-1-213509-3.
- [36] Gay, J.M. Stocker, P. and Rethore, F. 1993. "X-ray scattering studies of FeSi₂ films epitaxially grown on Si (111)." *Journal of applied physics*. 73(12) : 8169-8178.
- [37] Mahan, J.E. Thanh, V.L. Chevrier, J. Berbezier, I. Derrien, J. and Long, R.G. 1993. "Surface electron-diffraction patterns of β -FeSi₂ films epitaxially grown on silicon." *Journal of applied physics*. 74(3) : 1747-1761.
- [38] Rizzi, A. Rösen, B.N.E. Freundt, D. Dieker, C. Lüth, H. and Gerthsen, D. 1995. "Heteroepitaxy of β -FeSi₂ on Si by gas-source MBE." *Physical Review B*. 51(24) : 17780-17804.
- [39] Milosavljević, M. Shao, G. Bibić, N. McKinty, C.N., Jeynes, C. and Homewood, K.P. 2001. "Amorphous-iron disilicide: A promising semiconductor." *Applied Physics Letters*. 79(10) : 1438-1440.
- [40] Milosavljevic, M. Shao, G. Bibić, N. McKinty, C.N. Jeynes, C. and Homewood, K.P. 2002. "Synthesis of amorphous FeSi₂ by ion beam mixing." *Nuclear Instruments and Methods in Physics Research Section B: Beam Interactions with Materials and Atoms*. 188(1-4) : 166-169.

- [41] Li, X.N. Li, S.B. Nie, L.F. Li, H. Dong, C. and Jiang, X. 2010. "Preparation of amorphous $\text{Fe}_x\text{Si}_{1-x}$ film using unbalanced magnetron sputtering." *Thin Solid Films*. 518(24) : 7390-7393.
- [42] Milosavljević, M. Wong, L. Lourenço, M. Valizadeh, R. Colligon, J. Sha, G. and Homewood, K.P. 2010. "Correlation of structural and optical properties of sputtered FeSi_2 thin films." *Japanese Journal of Applied Physics*. 49(8R) : 081401-1-081401-11.
- [43] Milosavljević, M., Shao G., Lourenço M.A., Gwilliam R.M., Homewood, K.P. Edwards, S.P. Valizadeh, R. and Colligon, J.S. 2005. "Transition from amorphous to crystalline beta phase in co-sputtered FeSi_2 films as a function of temperature." *Journal of Applied Physics*. 98(12) : 123506-1-123506-6.
- [44] Nakamura, S. Aoki, T. Kittaka, T. Hakamata, R. Tabuchi, H. Kunitsugu, S. and Takarabe, K.I. 2007. "Facing target sputtered iron-silicide thin film." *Thin Solid Films*. 515(22) : 8205-8209.
- [45] Wasa, K. and Hayakawa, S. 1992. *Handbook of Sputter Deposition Technology: Principles, Technology, and Applications*. New Jersey : Noyes Publication.
- [46] Kadokura, S. Facing-targets-type sputtering apparatus and method. U.S. patent no. 6911123B2. June 2005.
- [47] Kadokura, S. Facing Target Type Sputtering Apparatus. U.S. patent no. 6156172. December 2000.
- [48] Yoshikawa, T. Facing Targets Sputtering Device. U.S. patent no. 5000834. March 1991.
- [49] Yuan, Y. and Lee, T.R. 2013. *Surface Science Techniques*. Berlin : Springer-Verlag Berlin Heidelberg.
- [50] Schrader, M.E. and Loeb, G.I. 2013. *Modern approaches to wettability: theory and applications*. Maryland, Springer Science & Business Media.
- [51] Mohamed, A.M. Abdullah, A.M. and Younan, N.A. 2015. "Corrosion behavior of superhydrophobic surfaces: A review." *Arabian Journal of Chemistry*. 8(6) : 749-765.
- [52] Bormashenko, E. 2015. "Progress in understanding wetting transitions on rough surfaces." *Advances in Colloid and Interface Science*. 222 : 92-103.
- [53] Wenzel, R.N. 1936. "Resistance of solid surfaces to wetting by water." *Industrial & Engineering Chemistry*. 28(8) : 988-994.
- [54] Cassie, A.B.D. and Baxter, S. 1944. "Wettability of porous surfaces." *Transactions of the Faraday society*. 40 : 546-551.

This material is reserved for educational use only, not allowed for commercial use.

Forbidden to modify the content, and cite the document when use.

- [55] Hashmi, S. 2017. *Comprehensive Materials Finishing*. Oxford : Elsevier.
- [56] Azizian-Kalandaragh, Y. Nouhi, S. and Amiri, M. 2015. "Effect of post-annealing treatment on the wetting, optical and structural properties of Ag/Indium tin oxide thin films prepared by electron beam evaporation technique." *Materials Express*. 5(2) : 137-145.
- [57] Yang, L. Zhang, M. Shi, S. Lv, J. Song, X. He, G. and Sun, Z. 2014. "Effect of annealing temperature on wettability of TiO₂ nanotube array films." *Nanoscale Research Letters*. 9(1) : 621-1-621-6.
- [58] Fanciulli, M. Zenkevich, A. Weyer, G. Vanzini, C. Tresso, E. and Baricco, M. 2001. "Structural and optical properties of Fe_{1-x}M_xSi₂ thin films (M= Co, Mn; 0 ≤ X ≤ 0.20)." *Microelectronic Engineering*. 55(1-4) : 233-241.
- [59] Kumar, A. Dalapati, G.K. Hidayat, H. Law, F. Tan, H.R. Widenborg, P.I. Hoex, B. Tan, C.C. Chi, D.Z. and Aberle, A. G. 2013. "Integration of β-FeSi₂ with poly-Si on glass for thin-film photovoltaic applications." *RSC Advances*. 3(21) : 7733-7738.
- [60] Tan, C.C. Dalapati, G.K. Tan, H.R. Bosman, M. Hui, H.K. Tripathy, S. and Chi, D. 2015. "Crystallization of sputter-deposited amorphous (FeSi₂)_{1-x}Al_x thin films." *Crystal Growth & Design*. 15(4) : 1692-1696.
- [61] Jia-Xiong, X. Ruo-He, Y. and Yu-Rong, L. 2011. "Fabrication of a ZnO: Al/Amorphous-FeSi₂ Heterojunction at Room Temperature." *Chinese Physics Letters*. 28(10) : 107304-1-107304-3.
- [62] Terai, Y., Haruki Y., Hiroaki, T. Tetsu, H. and Takahiko, H. 2014. "Effects of lattice deformations on Raman spectra in β-FeSi epitaxial films." In *JJAP Conference Proceedings (Vol. 3)*. The Japan Society of Applied Physics.
- [63] Drelich, J. Chibowski, E. Meng, D.D. and Terpilowski, K. 2011. "Hydrophilic and superhydrophilic surfaces and materials." *Soft Matter*. 7(21) : 9804-9828.
- [64] Krasowska, M. Zawala, J. and Malysa, K. 2009. "Air at hydrophobic surfaces and kinetics of three phase contact formation." *Advances in Colloid and Interface Science*. 147 : 155-169.
- [65] Lafuma, A. and Quéré, D. 2003. "Superhydrophobic states." *Nature materials*. 2(7) : 457-460.
- [66] Mortazavi, V. and Khonsari, M.M. 2017. "On the degradation of superhydrophobic surfaces: A review." *Wear*. 372 : 145-157.
- [67] Zaien, M. Ahme, N.M. and Hassan, Z. 2013. "Effects of annealing on the optical and electrical properties of CdO thin films prepared by thermal evaporation." *Materials Letters*. 105 : 84-86.

- [68] Senthilarasu, S., Sathyamoorthy, R., and Lalitha, S. 2004. "Synthesis and characterization of β -FeSi₂ grown by thermal annealing of Fe/Si bilayers for photovoltaic applications." *Solar Energy Materials and Solar Cells*. 82(1-2) : 299-305.
- [69] Liu, C. Yuan, Y. Jiang, J.T. Gong, Y.X. and Zhen, L. 2015. "Microwave absorption properties of FeSi flaky particles prepared via a ball-milling process." *Journal of Magnetism and Magnetic Materials*. 395 : 152-158.
- [70] Chaikereee, T. Nuchuay, P. Kasayapanand, N. Mungkung, N. Arunrungrusmi, S. Horprathum, M. Eiamchai, P. Limwichean, S. Patthanasettakul, V. Nuntawong, N. and Oros, C. 2017. "Enhanced transmission based on vertically aligned ITO NRs deposited by Ion assisted electron beam evaporation with glancing angle deposition technique." *Materials Today: Proceedings*. 4(5) : 6060-6064.
- [71] Ng, Z.N. Chan, K.Y. and Tohsophon, T. 2012. "Effects of annealing temperature on ZnO and AZO films prepared by sol-gel technique." *Applied Surface Science*. 258(24) : 9604-9609.
- [72] Cha, S.C. Her, E.K. Ko, T.J. Kim, S.J. Roh, H. Lee, K.R. Oh, K.H. and Moon, M.W. 2013. "Thermal stability of superhydrophobic, nanostructured surfaces." *Journal of Colloid and Interface Science*. 391 : 152-157.

Author Biography

Name	Mr.Peerasil Charoenyuenyao	
Date of Birth	04 March 1994	
Education	2016 Bachelor of Science in Physic	GPA 2.23
	King Mongkut's Institute of Technology Ladkrabang	
	2018 Bachelor of Science in Physic	GPA 3.50
	King Mongkut's Institute of Technology Ladkrabang	

Academic Publications

- 1) Peerasil Charoenyuenyao, Nathaporn Promros, Rawiwan Chaleawpong, and Tsuyoshi Yoshitake, Surface morphology and wettability for thin films of beta-iron disilicide produced through direct-current sputtering utilizing a pair of facing targets, The 4th International Conference on Engineering, Applied Sciences and Technology, 1091-1094.
- 2) Nathaporn Promros, Pitoon Noymaliwan, Peerasil Charoenyuenyao, Rawiwan Chaleawpong, Supanit Porntheeraphat, Bunpot Saekow, Tanapoj Chaikereee, Benjarong Samransuksamer, Peerapong Nuchuy, Chanunthorn Chananonnawathorn, Saksorn Limwichean, Mati Horprathum, Pitak Eiamchai, and Viyapol Patthanasettakul, Study of Annealing Influence on Basic Properties of Indium Tin Oxide Nanorod Films Deposited Using Glancing Angle Ion-Assisted Electron Beam Evaporation, Journal of Nanoscience and Nanotechnology, (accepted). (Impact factor 1.483, Indexed in-ISI)
- 3) Rawiwan Chaleawpong, Nathaporn Promros, Peerasil Charoenyuenyao, Takanori Hanada, Shinya Ohmagari, Abdelrahman Zkria, and Tsuyoshi Yoshitake, Junction Parameters of Boron-Doped p-Type Ultrananocrystalline Diamond/Hydrogenated Amorphous Carbon Composite/n-Type Silicon Heterojunctions Formed by Pulsed Laser Deposition, Journal of Nanoscience and Nanotechnology, (accepted). (Impact factor 1.483, Indexed ISI)
- 4) Weerasaruth Kaenrai, Nathaporn Promros, Phongsaphak Sittimart, Rawiwan Chaleawpong, Peerasil Charoenyuenyao, Thanachai Changcharoen, Adison Nopparuchikun, Tomohiro Nogami, and Tsuyoshi Yoshitake, Photovoltaic

This material is reserved for educational use only, not allowed for commercial use.

Forbidden to modify the content, and cite the document when use.

Properties and Series Resistance of p-Type Si/Intrinsic Si/n-Type Nanocrystalline FeSi₂ Heterojunctions Created by Utilizing Facing-Targets Direct-Current Sputtering, *Journal of Nanoscience and Nanotechnology*, (accepted). (Impact factor 1.483, Indexed in ISI)

- 5) Nathaporn Promros, Pitoon Noymaliwan, Peerasil Charoenyuenyao, Rawiwan Chaleawpong, Supanit Porntheeraphat, Bunpot Saekow, Tanapoj Chaikereee, Benjarong Samransuksamer, Peerapong Nuchuay, Chanunthorn Chananonnawathorn, Saksorn Limwichean, Mati Horprathum, Pitak Eiamchai, and Viyapol Patthanasettakul, Impact of Annealing Temperature on the Physical Properties of Indium Tin Oxide Nanorod Films Grown by Glancing-Angle Ion-Assisted Electron-Beam Evaporation, *E-MRS Proceedings*, (accepted).

